Phase Selection During Solidification and Solid-State Phase Transformations in an Al-10Ce-8Mn (wt.%) Alloy.

Kevin Sisco[1], Alex Plotkowski[2], Thomas Feldhausen[3,4], Suresh Babu[1,3]

[1]Mechanical, Aerospace and Biomedical Engineering, University of Tennessee – Knoxville

[2]Materials Science & Technology Division, Oak Ridge National Laboratory

[3]Manufacturing Science Division, Oak Ridge National Laboratory

[4]The University of Texas - El Paso, TX

1 Abstract

In multicomponent Al-Ce alloys, and especially after additive manufacturing (AM), complex and metastable solidification microstructures are frequently observed. In this research, the relationship between solidification conditions and phase selection are explored for an Al-10Ce-8Mn (wt.%) alloy using a systematic study of laser melting conditions. Three solidification modes were observed: primary $Al_{10}Mn_2Ce$; primary $Al_{20}Mn_2Ce$; and eutectic FCC Al + $Al_{20}Mn_2Ce$. These solidification modes were correlated to specific solidification velocities using a simple thermal model, showing the change in primary solidification phase for low (<$6.8x10^{-4}$ m/s), moderate (between $8.2x10^{-4}$ and $5.9x10^{-2}$ m/s) and high solidification velocities (>$6.2x10^{-2}$ m/s) for the above three solidification microstructures, respectively. These results were rationalized by using interface response function (IRF) theory to describe the solidification undercooling for the possible primary intermetallic phases. The implication of the local phase selection from differing solidification conditions is summarized by a comparison of hardness which demonstrates the potential variance of Vickers hardness from 101 to 242 (VHV) by changing the laser velocity from 1 to 83 mm/s. Interestingly, on heat treatment at 400°C, the decomposition pathways of the solidification microstructure and hardness were also found to be different, thereby opening multiple pathways for spatial microstructure and property control within AM components.

2 Introduction

Metal additive manufacturing (AM) processes produce unique microstructures by overlapping weld tracks in the same plane and stacking weld tracks on top of each other to produce a part [1]. The microstructures produced by these processes are the result of rapid solidification conditions in each weld track, where high solidification (liquid/solid interface) velocities (R) and thermal gradients (G) are present. The controlled solidification conditions can enable localized tailoring of microstructures [2–4] and properties [please refer to Sumit's paper]. This is achieved by manipulating the processing parameters of the AM machine spatially and temporally in a given layer, which modifies the weld pool

dynamics and can lead to variation in G and V spanning several orders of magnitude. Several examples in nickel super alloys took advantage of different processing conditions to achieve spatial control of columnar and equiaxed grain morphologies and associated textures [2,5–7].

Despite the advantages of AM, high strength age-hardening aluminum alloys are prone to processing defects such as solidification cracking and gas-induced porosity, which result from local weld track conditions [8,9]. Although the extent of porosity can be reduced, the reduction of solidification cracking has been elusive due to large changes in thermomechanical conditions during rapid solidification, and large freezing ranges with dilute compositions. Therefore, extensive efforts are underway to develop a new generation of Al-alloys that are resistant to solidification cracking either by reducing the solidification range or by adding inoculating agents to refine the grain size [10,11]. The Al-10Si-0.5Mg alloy (wt.%), for example, has reduced solidification cracking tendency due to its small freezing range [12–16]. However, there is a challenge in adopting the Al-10Si-0.5Mg (wt.%) alloy due to the degradation of tensile strength at elevated temperatures. Takata et al. [17] showed that the tensile strength of this alloy decreased by 190 MPa after annealing at 300°C for 2 hours. As a result, the Al-10Si-0.5Mg alloy has become unsuitable for elevated temperature applications [9]. Another challenge for high strength aluminum alloys (e.g., 2XXX, 6XXX, 7XXX series) which commonly include Mg and Zn, is the vaporization of secondary elements. The vaporization can occur during AM because of the low boiling points and high vapor pressures of Mg and Zn (1091 and 907°C respectively) compared to the high boiling point (2470°C) and low vapor pressure of Al [18–20], which can result in changes to the alloy composition. Another effect of excessive evaporation is also to the formation of keyholes and associated pores. While it is possible to select processing parameters that avoid solidification cracking and keyhole porosity, to do so limits the available process parameter window to achieve dense parts [18]. Therefore, new Al alloys are being examined that can take advantages of the unique processing of AM while minimizing processing related defects.

In the literature, the Al-Ce binary system is of interest because it has been shown to be resistant to solidification cracking [21] during casting. This alloy solidifies with a fine eutectic microstructure between FCC Al and $Al_{11}Ce_3$ (Immm) [21], and is resistant to coarsening of secondary phases during subsequent exposure to elevated temperatures [22–25]. For example, an Al-10Ce (wt.%) alloy showed an increase in yield strength (50 MPa Cast, 222.1 MPa AM at 23°C) and ultimate tensile strength after AM, in comparison to casting (152 MPa Cast, 319.3 MPa AM at 23°C) [21,26]. Similar improvements in mechanical properties were also observed as we transition from casting to AM in an Al-Cu-Mn-Zr alloy [27]. A second study on the same alloy concluded that the increase in strength was a result of the refinement of the Al_2Cu (θ) intermetallic particles, the θ particles had increased lattice strain states during tensile testing in the AM samples compared to casting, determined by high energy x-ray diffraction [28]. In addition to binary Al-Ce alloys, higher order Al-Ce-X alloys have been investigated [29–32]. One of these alloys is Al-Ce-Mg alloy and AM conditions lead to the formation of a metastable phase, specifically, $Al_{13}CeMg_6$ [30]. Similar results of metastable phase formation resulting from changes in local solidification conditions have been observed during AM processing of Al-Cu-Ce, Al-Ce-Ni-Mn, and Al-Ce-Mn alloys [29,33,34]. The challenge with the formation of metastable phases is that they can decrease the stability of a microstructure during high temperature service leading to early failure of components made by AM. Therefore, it is important to understand why and when metastable phases form so that it is possible to manipulate local mechanical properties for improved performance in

future. The manipulation of local properties has previously been shown in an Al-Cu-Ce-Zr eutectic alloy by Bahl *et. al.* [35], where the local hardness was controlled by manipulating the laser velocity.

The current work focuses on microstructure evolution during solidification in an Al-Ce-Mn alloy. The Al-Ce-Mn system was used because the primary phase selection during solidification can vary due to local changes in G and R. In a study by Yang *et al.* [36], the primary solidification phase was observed to be $Al_{10}Mn_2Ce$, followed by a combination of $Al_{20}Mn_2Ce$, FCC Al and $Al_{11}Ce_3$ in samples made by arc melting and solidification in a copper mold of an Al-9.0Ce-6.2Mn (wt.%) alloy. In an another example, Gordillo *et al.* [37] observed primary solidification of $Al_{20}Mn_2Ce$, followed by FCC Al, Al_6Mn, and $Al_{11}Ce_3$ in gas atomized powder of an Al-9Ce-9Mn (wt.%) alloy. It is well known that the gas atomization conditions may lead to large changes in cooling rate (10^4 to 10^5 K/s) as a function of particle diameter [38,39]. Plotkowski *et al.* [32] also observed the primary $Al_{20}Mn_2Ce$ intermetallic compound at the weld-pool boundaries followed by FCC Al and $Al_{11}Ce_3$ in a weld track produced using L-PBF. However, as the solidification velocity increased towards the center of the weld track, the primary $Al_{20}Mn_2Ce$ was suppressed and a eutectic between FCC Al and $Al_{20}Mn_2Ce$ emerged. This transition was attributed to spatial changes in G and R within the melt pool. These three studies demonstrated that the initial phase selection is very sensitive to local solidification conditions. However, the above published works are qualitative. Therefore, in this research, we attempted to quantify the transition between phase selection and demonstrate the consequences on mechanical behavior.

The effect of solidification conditions on phase selection has been previously explored in Al-Cu [40,41], Fe-Cr-Ni systems [42,43] and other alloys in the welding metallurgy literature. The prediction of phase selection based on solidification conditions is possible using interface response function (IRF) models [40–42,44–50]. The IRF models predicts the undercooling of a phase growth during solidification in response to local G and R. Furthermore, the IRF models have been extended to describe planar, dendritic, and eutectic solidification modes.

It is also well known that the solid-state phase decomposition of the as-solidified microstructure is sensitive to the composition of pre-existing phases and their respective morphologies. Yang *et al.* [36] showed that on heat treatment at 350°C, the primary $Al_{10}Mn_2Ce$ did not decompose, but the primary $Al_{20}Mn_2Ce$ decomposed into $Al_{10}Mn_2Ce$. Gordillo *et al.* [37] showed that these decomposition pathways are sensitive to thermomechanical history. For example, he performed heat treatment on samples at 350°Cm where the samples were obtained by extruding the atomized powder from a canned billet preheated to 310°C using a preheated 4500-ton press. In these samples, the primary $Al_{20}Mn_2Ce$ phase decomposed fully into a combination of FCC Al, $Al_{11}Ce_3$ and $Al_{12}Mn$ after heat treatment at 400°C for 96 hours. In the case by Plotkowski et al. [32] and further work by Sisco et al. [51], the primary $Al_{20}Mn_2Ce$ produced by AM decomposed into a combination of FCC Al, $Al_{11}Ce_3$, Al_6Mn, and $Al_{12}Mn$ on heat treatment at a temperature range of 350 to 450°C. Furthermore, the eutectic between FCC Al and $Al_{20}Mn_2Ce$, decomposed into an $Al_{51}Mn_7Ce_4$ phase. The above work suggests that the site-specific microstructure of the Al-Ce-Mn system can be achieved by changing local solidification conditions, similar to what is observed in AM of Ni super alloys [2,5–7].

In this study, the goal is to quantify the link between processing conditions, local solidification conditions and the resultant solidification microstructure and solid-state decomposition pathways. A generalized IRF model is used to predict the phase selection as a function of local solidification

conditions (G and R) using laser weld tracks by manipulating in an Al-10Ce-8Mn (wt.%) alloy. The changes in solidification phase selection will be rationalized by reexamining the dendritic interface response function [40,41,45–47,52] and modifying the IRF for intermetallic compounds that exhibit non-linear thermodynamic liquidus slopes. The analysis focuses on the transition from primary $Al_{10}Mn_2Ce$ to primary $Al_{20}Mn_2Ce$ and then to a eutectic microstructure consisting of FCC Al and $Al_{20}Mn_2Ce$. These transitions are experimentally determined with weld tracks performed under controlled conditions, and the dendritic IRF will be fit to experimental observations. To evaluate the reproducibility of the solid-state decomposition of metastable solidification microstructure, the samples were also characterized after heat treatments at 400°C for 96 hours and the results are compared with existing literature.

3 Methods

3.1 Modeling Thermal Conditions in Weld Tracks

The Rosenthal model [54] for quasi-static heat conduction around a moving point source was used to estimate the thermal conditions within each melt pool. The thermophysical properties used in the Rosenthal model were approximated from a few assumptions. The first is that the thermal conductivity is largely controlled by the amount of Mn in solid solution. In the AM base material, the Mn content varies from 0.228 (at.%) to 1.688 (at.%) [51], here we use a thermal conductivity corresponding to a Mn content of 0.49 (at.%) from Zhang et al. [55]. The specific heat was taken from an Al-10Si-Mg alloy [55]. The density was calculated based on the alloy composition. The edge of the melt pool boundary is expected to be at the melting point of the $Al_{20}Mn_2Ce$ phase, 1177 K, for the bulk composition Al-10Ce-8Mn (wt.%). This temperature was calculated using PANDAT [56,57] software.

Table 1 Thermophysical properties used in the Rosenthal model.

Thermophysical Properties		Source
Specific Heat (J/kg-K)	920	Al-10Si-Mg [58]
Thermal Conductivity (W/K-m)	120.17	Zhang et al. [55]
Density (kg/m^3)	3034	Calculated
$T_{isotherm}$ (K)	1177	PANDAT [36,56,57]

The absorption efficiencies for each model were calibrated by matching the predicted depth to the measured depth. The depth of each weld track was determined by measuring the SEM-BSE data from the top of the weld track to the base of the weld track. This measurement included both the partially melted zone (PMZ) and the melt pool boundary (MPB). The PMZ and MPB were characterized using the predicted temperature distribution from the Rosenthal equation [54]. An example of the separation of PMZ and MPB is shown in Figure 1. The temperature at the edge of the partially melted zone was

assumed to be the eutectic temperature for FCC Al and $Al_{20}Mn_2Ce$ at 927 K. The laser absorptivity (shown in Table 4) was fit to the depth of the 927 K isotherm, and then the 1177 K isotherm (the liquidus temperature of $Al_{20}Mn_2Ce$) was extracted at the same laser absorptivity. The width of the PMZ was approximated by the distance between the two isotherms. The solidification conditions in the weld tracks were calculated at the 1177 K isotherm.

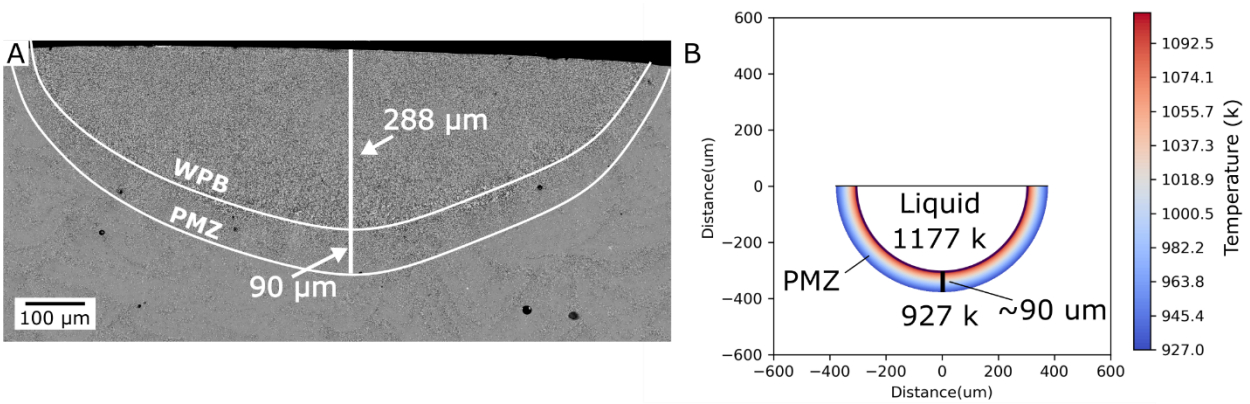

Figure 1 shows an example of the deduction of weld track depth for the 54 mm/s weld track. (A) shows the predicted weld pool depth and partially melted zone width for a fit laser absorptivity, and (B) is a projection of the temperature distribution of the Rosenthal model on the y, z plane that is plotted between the 927 and 1177 K isotherms (the freezing range of the bulk composition).

3.2 Modification of Interface Response Function for Non-Linear Liquidus Slopes

Interface response functions (IRFs) have been used to understand the selection of a particular growth mode during solidification [40–42,44–50] as a function of solidification condition (i.e., solidification velocity, thermal gradient, and composition). Furthermore, the IRF models can also describe the transitions between planar, dendritic, and eutectic growth during solidification. In the current work, only the dendritic solidification model is explored because of its relevance to the selection of the relevant intermetallic phases. The eutectic growth model is relevant, but current theories do not have extensions from binary to higher order systems. Therefore, the eutectic growth was assumed to occur at the eutectic temperature, 927 K where the liquid transforms into the solid $Al_{20}Mn_2Ce$ and FCC Al phases.

The premise of the dendritic IRF is to calculate the dendrite tip undercooling, ΔT_{tot}, for dendritic growth of a phase with five key contributions:

$$\Delta T_{tot} = \Delta T_T + \Delta T_R + \Delta T_C + \Delta T_K + \Delta T_{Cell}$$	*(1)*

where ΔT_R the undercooling due to the Gibbs-Thomson Effect (curvature), ΔT_C the constitutional (solutal) undercooling, ΔT_K the undercooling for attachment kinetics from the liquid to the solid, ΔT_{Cell} is the cellular undercooling at low interface velocities, and ΔT_T is the thermal undercooling. ΔT_T, the

undercooling required to transport the latent heat of fusion away from the dendrite tip, is ignored as the large thermal gradients in the solid phase are assumed to conduct latent heat away from the solid/liquid interface quickly into the solid phase, minimizing the impact of the latent heat on total undercooling.

The dendritic IRF is commonly solved using a linear phase diagram approximation. More information about the dendritic IRF approximation is given in Appendix 8.2.

In the current research, the linear approximation of the IRF was determined to be inadequate due to the large curvature of the liquidus slopes in the Al-Ce-Mn system. Preliminary calculations using the linear approximation significantly under- or over-predicted the undercooling of a phase based on initial conditions. Therefore, instead of the linearized approximation of the liquidus slope and constant partition coefficient, the liquidus slope and partition coefficients are determined using PANDAT at the composition of the dendrite tip during each iteration. A similar approach was attempted for the Ag-Cu system by others [48]. In this publication, coefficients of polynomial equations were fit to the liquidus line and partition coefficient. However, we propose that direct coupling of the IRF to PANDAT is preferred for a more generalized and consistent solutions for calculating the liquidus slope, m_i, and partition coefficient, k_0^i, of each element at the composition of the dendrite tip for wide range of alloy compositions. The above methodology for calculating constitutional undercooling, ΔT_c was implemented using the PANDAT SDK [56,57]. PANDAT, a CALPHAD solver, calculated the equilibrium condition consistent with the composition in the liquid at the dendrite tip. Then, the ΔT_c was defined to be the difference in liquidus temperatures predicted at the bulk composition and that is calculated at the composition of the dendrite tip.

$$\Delta T_C = f(C_{0,Mn},C_{0,Ce}) - f(C_{t,Mn},C_{t,Ce}) \quad (2)$$

Where $f(C_{0,Mn},C_{0,Ce})$ is the liquidus temperature at the bulk composition, and $f(C_{t,Mn},C_{t,Ce})$ is the liquidus temperature at the composition of the dendrite tip. A list of inputs used for the dendritic IRF calculation of various phases is given in Table 2. More information about how the interface response function is coupled with PANDAT is described in Appendix 8.3.

Table 2 Parameters used in the IRF Calculations for $Al_{10}Mn_2Ce$ and $Al_{20}Mn_2Ce$

Parameters	$Al_{20}Mn_2Ce$	$Al_{10}Mn_2Ce$	Sources
Initial Ce Composition, $C_{0,Ce}$ (at. %)	2.18	2.18	Given
Initial Mn Composition, $C_{0,Mn}$ (at. %)	4.48	4.48	Given
Gibbs-Thomson Coefficient (m-k)	$1.x10^{-6}$ (Fit)	$1.57x10^{-6}$ (Fit)	Fit to Experimental Data
Liquid Diffusivity of Mn, D_L^{Mn} (m^2/s)	3.34×10^{-9}	3.34×10^{-9}	Du *et al.* [59]
Liquid Diffusivity of Ce, D_L^{Ce} (m^2/s)	2.5×10^{-9}	2.5×10^{-9}	Assumed
Dendrite Tip Selection Parameter σ	0.025	0.025	Dantzig and Rappaz [50]
Thermal Gradient (K/m)	$1x10^6$	$1x10^6$	Assumed
Speed of Sound in FCC Al, V_0 (m/s)	5100	5100	Assumed as FCC

3.3 Sample Production

Samples were produced in two stages. Initially, a cylindrical (15 mm diameter and 115 mm height) sample was produced in laser powder bed fusion (L-PBF) using the procedure described by Plotkowski et al. [32]. The composition of the L-PBF sample was measured using inductively coupled plasma technique and found to be Al-10Ce-8Mn (wt.%). This cylinder was sectioned into 5 mm disks perpendicular to the build direction. The surface of the sample was scoured with eight hundred grit grinding paper to achieve a consistent surface finish. Then, single-track laser welding experiments were performed on this surface using an Okuma MU-8000V-L LASER EX machine. The process parameters are summarized in Table 3. These parameters were chosen to transition from high (200 J/mm) to low (6 J/mm) heat input conditions, which in turn affects the cooling rate [53]. Welding was performed with Argon shielding. After remelting, the samples were cross-sectioned perpendicular to the direction of the laser track. One half of the track was characterized in the as solidified state, and the other half was characterized after heat treatment at 400°C for 96 hours.

Table 3 Laser track processing parameters

Sample I.D.	Power (W)	Laser Velocity (mm/s)	Spot Size (mm)	Heat Input (J/mm)
1	200	1	1.5	200.00
2	500	10	1.5	50.00
3	500	15	1.5	33.33
4	500	23	1.5	21.74
5	500	35	1.5	14.29
6	500	54	1.5	9.26
7	500	83	1.5	6.02

3.4 Material Characterization

Samples were characterized by scanning electron microscopy (SEM) using backscatter electron detector (BSE) detector in a Zeiss Gemini Crossbeam instrument. The Images were collected at an accelerating voltage of 5 kV and a current of 3000 nA. The use of a BSE detector allows for the differentiation of various phases based on the z-contrast which strongly depends on elemental concentration such as cerium.

Vickers hardness measurements were preformed using a LECO AMH 55 Automatic Hardness tester. Local hardness measurements were taken using a 50-gram load and a 10 second dwell time. The spacing between measurements was adjusted to compensate for the differences in depth of each weld track.

4 Results

4.1 Thermal Modeling

Using the method described in Figure 1, the laser absorption efficiencies for the Rosenthal model was calibrated to the depth of each weld track. The results are summarized in. The absorption efficiency is not constant across samples and tends to decrease with a decrease in heat input. Note that the absorption efficiency is dependent on a variety of effects such as the melt pool shape, internal reflections, radiation, and vaporization losses, which are not accounted for in the Rosenthal model

[54,60]. Additionally, the increase in laser absorption tends to increase with power density because of deepening of the possible formation of a vapor cavity, which increases internal reflections [61].

Table 4 Measurement of the weld track depth for each laser velocity.

Weld Track	Laser Velocity (mm/s)	Weld Track Depth (μm)	Calibrated Laser Absorption	PMZ Width (μm)
1	1	271	0.712	82
2	10	540	0.551	142
3	15	518	0.545	134
4	23	461	0.502	116
5	35	425	0.487	104
6	54	378	0.467	90
7	83	326	0.44	73

Using the calibrated absorption efficiencies, the solidification velocity and thermal gradient were calculated for each weld track (Figure 2). Based on previous work, the absorption efficiency of the AM sample with parameters taken from [32] was assumed to be 0.33. The results from the Rosenthal model give a range of thermal gradients (~$1x10^6$ to ~$1x10^7$ K/m) and solidification velocities (~$1x10^{-5}$ to ~0.1 m/s) from the weld track experiments. From the range of thermal characteristics predicted by the Rosenthal model, the 1, 10 and 83 mm/s laser velocity weld tracks were selected for further characterization because of the coverage over the solidification conditions of interest. In the weld track calculations, the highest thermal gradient and lowest solidification velocity will exist at the edge of the weld track. The lowest thermal gradient and highest solidification velocity will exist at the centerline of the weld track [62]. More information about the Rosenthal model is described in Appendix 8.4.

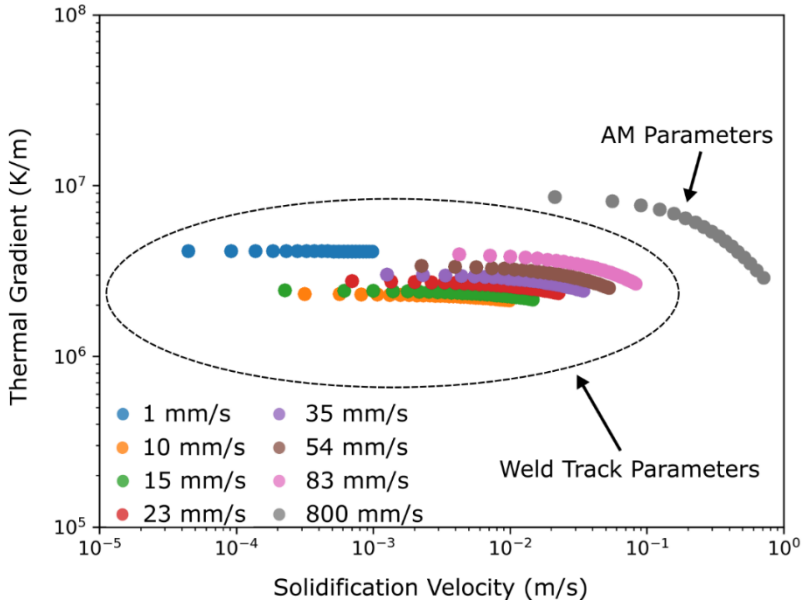

Figure 2 plots the output of solidification velocity and thermal gradient from the point source Rosenthal model for each weld track parameter and the AM parameter from Plotkowski et al. [32]*. The model parameters are outlined in Table 3 and Solidification Phase Selection*

SEM BSE micrographs of the as-printed weld track 1 (see Table 3) are shown in Figure 3. Figure 3A is an overview image from the base of the weld track, including the partially melted zone (PMZ), the weld pool boundary (WPB), and the top of the weld track (TWT). In the SEM-BSE images, in which z-contrast is dominant, phases appear in the order of brightest to darkest: $Al_{11}Ce_3$, $Al_{10}Mn_2Ce$, $Al_{20}Mn_2Ce$, and FCC Al, respectively. Figure 3B shows an example microstructure near the WPB. Near the WPB, the primary $Al_{10}Mn_2Ce$ phase was observed. Surrounding the $Al_{10}Mn_2Ce$ was FCC Al, $Al_{20}Mn_2Ce$ and $Al_{11}Ce_3$. (See appendix 8.1 for phase identification using Kikuchi diffraction.) At distances further from the edge of the weld pool, which correspond with higher solidification velocity from the Rosenthal model, the $Al_{20}Mn_2Ce$ phase was observed and $Al_{10}Mn_2Ce$ was no longer present. The primary $Al_{20}Mn_2Ce$ phase was observed to be present until the top of the weld track as seen in Figure 3D. In between the primary $Al_{20}Mn_2Ce$ phase is FCC Al and $Al_{11}Ce_3$.

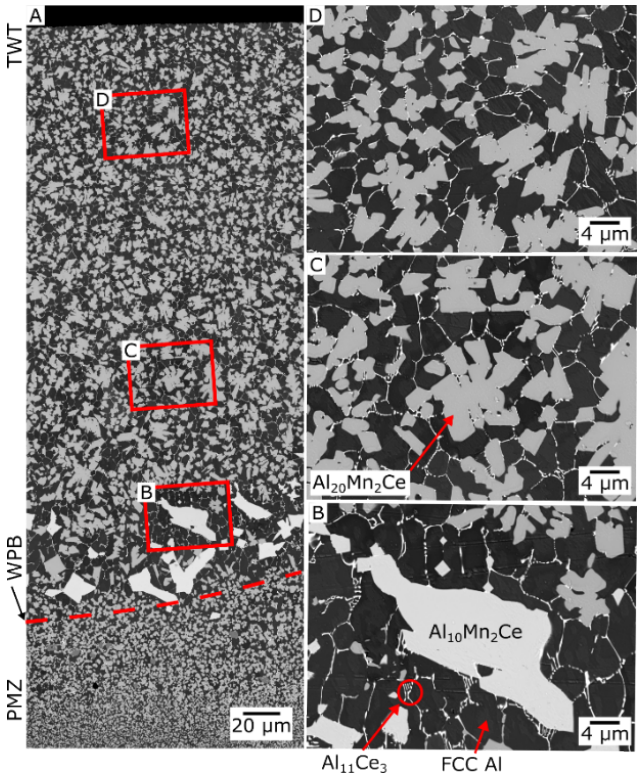

Figure 3 SEM BSE of the 1 mm/s weld track. Where (A) is the overview of the weld track, (B) is a microstructure near the WPB, (C) is an example microstructure away from the WPB, and (D) is a microstructure near the top of the weld track.

SEM BSE micrographs of weld track 2 are shown in Figure 4. Figure 4A is an overview image from the base of the weld track, including the PMZ, the WPB, and TWT. The $Al_{10}Mn_2Ce$ was observed sparsely near the weld pool boundary. Slightly away from the WPB, the $Al_{10}Mn_2Ce$ was suppressed in favor of the formation of primary $Al_{20}Mn_2Ce$. Figure 4C shows an example microstructure away from the WPB that shows a primary $Al_{20}Mn_2Ce$ phase surrounded by FCC Al and $Al_{11}Ce_3$. Figure 4D shows an example microstructure near the top of the weld track, where the primary solidification phase was observed to be $Al_{20}Mn_2Ce$.

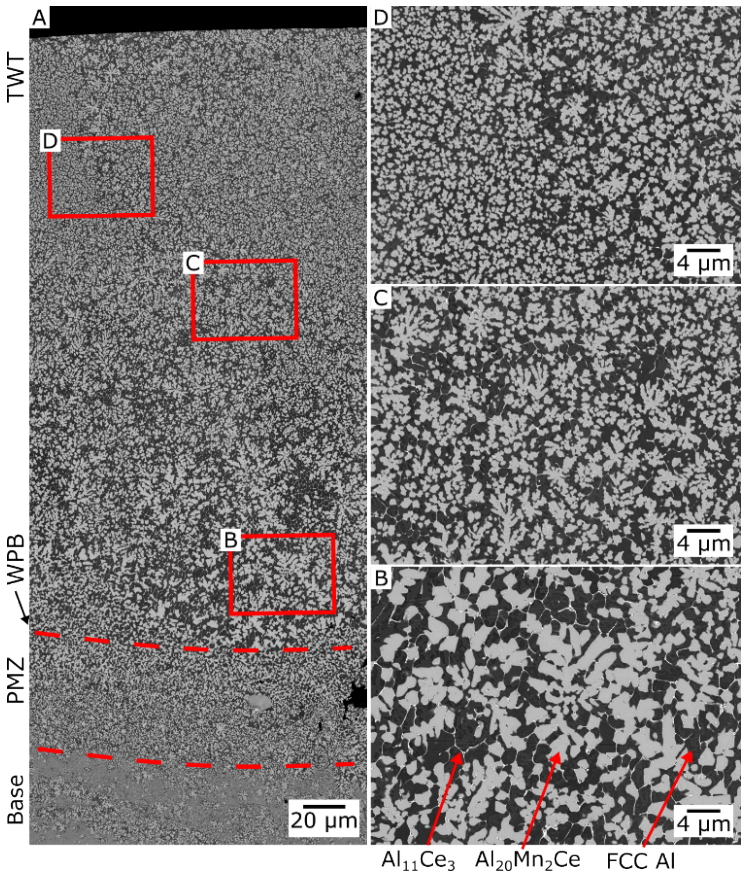

Figure 4 SEM BSE of the 10 mm/s weld track. Where (A) is an overview of the microstructure, (B) is a representative microstructure near the WPB, (C) is a representative microstructure near the middle of the weld track, and (D) is a representative mcirostructure near the top of the weld track. Each region above the weld track is observed to contain FCC Al, $Al_{20}Mn_2Ce$, and $Al_{11}Ce_3$ identifed using SEM BSE.

Figure 5 is an overview of the microstructure from the lowest heat input weld track 7, including the PMZ, the WPB, and the TWT. Figure 5B shows an example microstructure near the WPB, which contains primary $Al_{20}Mn_2Ce$, FCC Al, and $Al_{11}Ce_3$. Figure 5C shows an example microstructure away from the WPB, where the primary $Al_{20}Mn_2Ce$ was suppressed, forming instead a lamellar eutectic microstructure containing FCC Al and $Al_{20}Mn_2Ce$. Figure 5D shows an example microstructure near the TWT which demonstrates the eutectic transitioning back into the primary $Al_{20}Mn_2Ce$. The transitions in phase selection are a result of complex heat transfer and fluid flow conditions that can locally change the solidification conditions and transport of un-melted particles, which is not discussed in the current work.

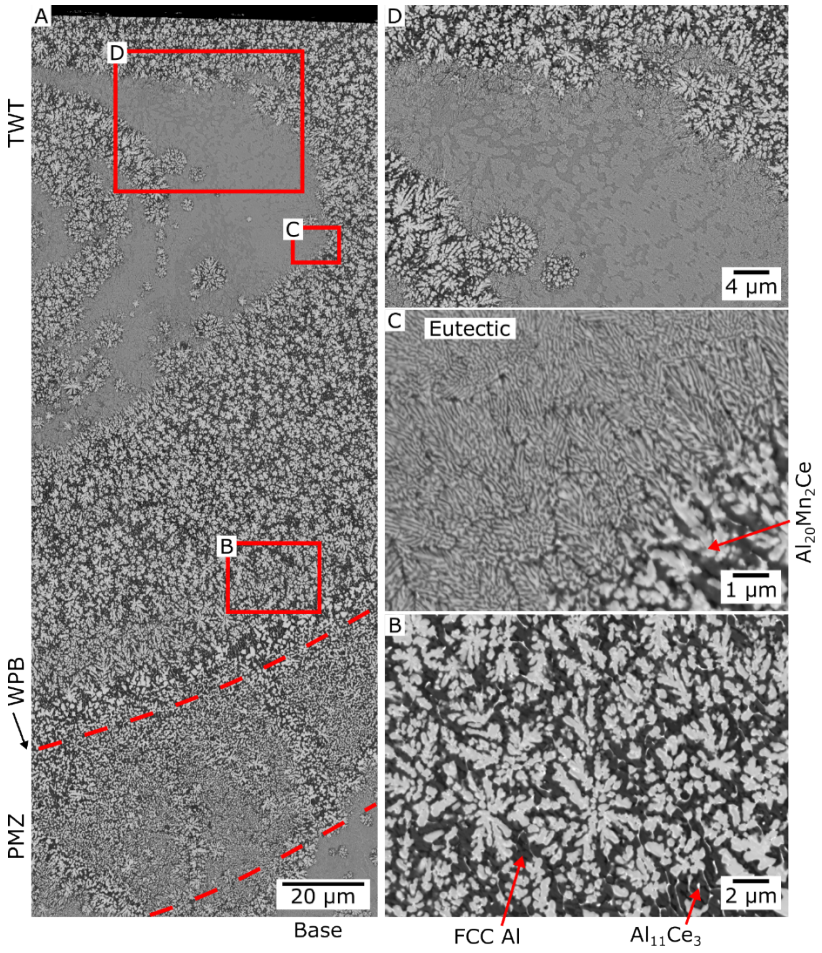

Figure 5 SEM BSE of the 83 mm/s weld track. Where (A) is an overview of the microstructure, (B) is a representative microstructure near the WPB, (C) is a representative microstructure near the middle of the weld track, and (D) is a represnetative mcirostructure near the top of the weld track. Each region above the weld track is observed to contain FCC Al, $Al_{20}Mn_2Ce$, and $Al_{11}Ce_3$ identifed using SEM BSE.

4.2 Solid State Decomposition

The SEM micrographs of weld track 1 after heat treatment at 400°C for 96 hours are shown in Figure 6. Figure 6B shows an example microstructure near the WPB, in which the presence of $Al_{10}Mn_2Ce$ is confirmed. This phase has a similar morphology as the one see in the as-solidified region. Figure 6C shows an example microstructure away from the WPB, in which the regions surrounding $Al_{20}Mn_2Ce$ were partially decomposed. Figure 6D shows an example microstructure near the middle of the weld track in which the edges of the primary $Al_{20}Mn_2Ce$ were observed to decompose into $Al_{11}Ce_3$ and an unidentified phase. In a comparison with literature [32,37,51,63] and based on the contrast from SEM-BSE, the newly formed phases in this region are likely to be $Al_{11}Ce_3$ and an Al-Mn binary phase, such as Al_6Mn or $Al_{12}Mn$.

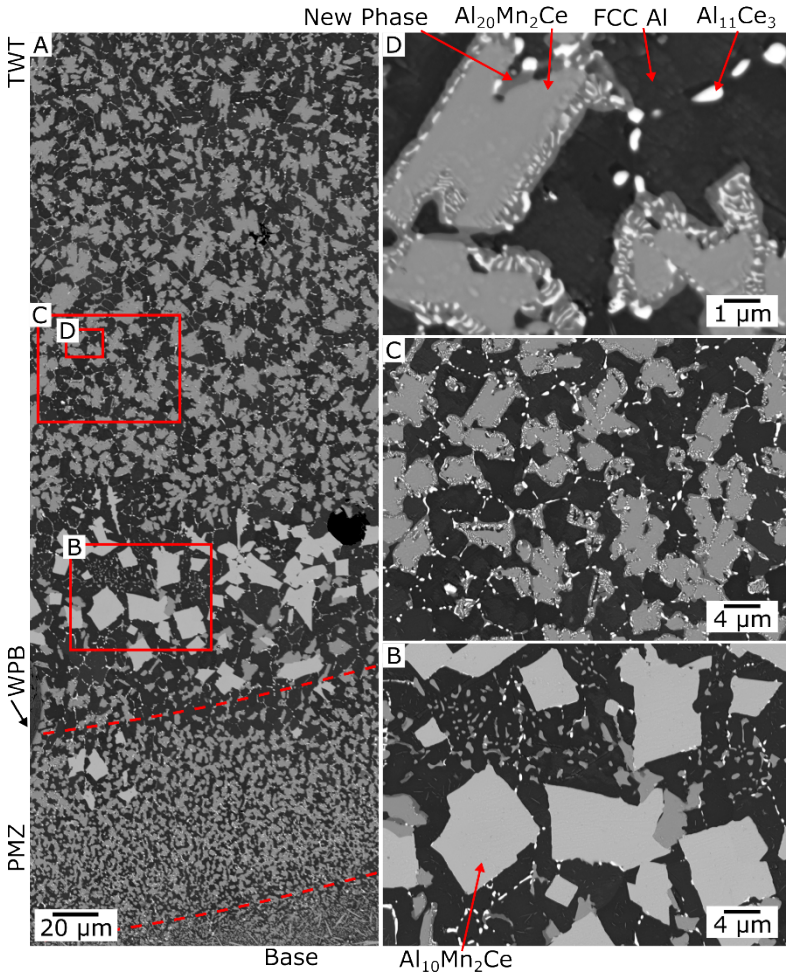

Figure 6 SEM BSE of the 1 mm/s weld track heat treated at 400°C for 96 Hours. Where (A) is an overview of the microstructure, (B) is a representative microstructure near the WPB, (C) is a representative microstructure near the middle of the weld track, and (D) is a high resolution region of the middle of the weld track.

SEM micrographs of the weld track 7 heat treated at 400°C for 96 hours shows dramatic changes (see Figure 7) compared to earlier results. We used the same convention as before to describe the microstructures, i.e., an overview image (Figure 7A) outlining the PMZ, the WPB, and the TWT. Above the WPB (Figure 7B), the $Al_{20}Mn_2Ce$ was partially decomposed into $Al_{11}Ce_3$ and Al-Mn binary phases, similar to the decomposition path observed in weld track 1. The prior eutectic region is shown in Figure 7C, shows the formation of a phase with plate morphology, similar to the one published in literature [32,64]. In the literature this plate like phase is identified as $Al_{51}Mn_7Ce_4$. At the top of the weld track, the eutectic microstructure transitioned back into primary $Al_{20}Mn_2Ce$. This result is similar to the as-deposited sample. In the heat-treated sample, the decomposition of the primary $Al_{20}Mn_2Ce$ appears to follow the previously observed decomposition pathway into $Al_{11}Ce_3$ and Al-Mn binary phases. However, intermixed throughout the decomposition of the primary $Al_{20}Mn_2Ce$ in the welds made with velocity ranging from 10 to 83 mm/s samples, we observed the plate phase. These results suggest that the solidification velocity and thermal gradient are playing a role in the decomposition pathway of the primary $Al_{20}Mn_2Ce$ phase.

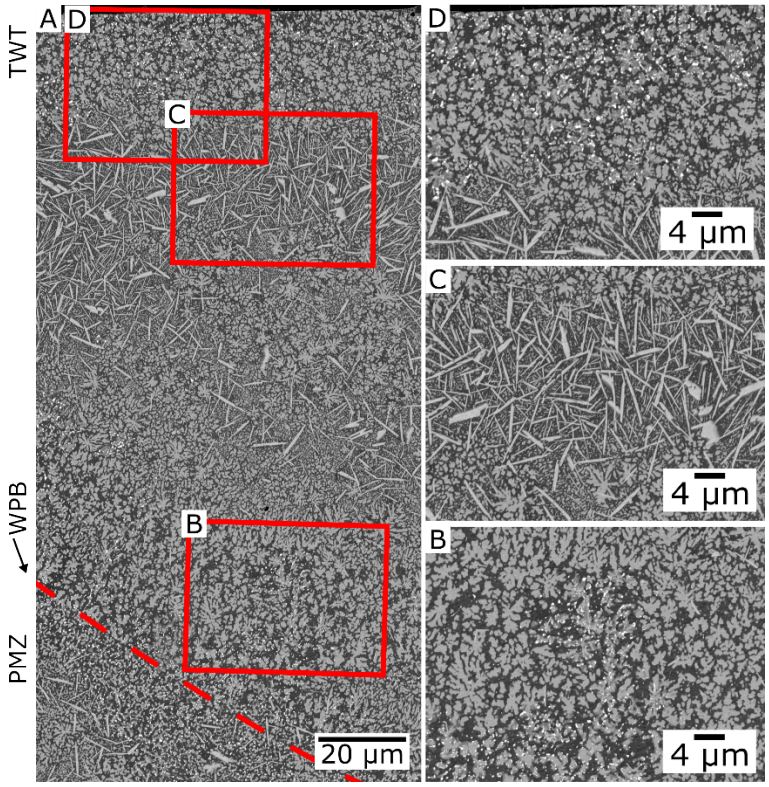

Figure 7 SEM BSE of the 83 mm/s weld track heat treated at 400°C for 96 Hours. Where (A) is an overview of the microstructure, (B) is a representative of the WPB decomposition pathways, (C) represents the eutecitc solidification decomposition pathway, and (D) represents the decomposition occuring at the top of the weld track.

5 Discussion

5.1 Solidification Phase Selection

In literature, the phase selection phenomena in the Al-Ce-Mn system have been observed as a function of solidification conditions during casting, powder making and AM. In microstructures from casting, Yang et al. [36] observed the formation of primary $Al_{10}Mn_2Ce$. In AM, Plotkowski et al. [32] observed the suppression of $Al_{10}Mn_2Ce$, and the formation of primary $Al_{20}Mn_2Ce$ and a eutectic between FCC Al and $Al_{20}Mn_2Ce$. In this work, the goal is to understand the transition between the primary phases and eutectic solidification. Therefore, the average distances from the weld pool boundary (WPB) to the transition regions at which the transitions from the (a) primary $Al_{10}Mn_2Ce$ to primary $Al_{20}Mn_2Ce$ phase and then from the (b) $Al_{20}Mn_2Ce$ phase to the eutectic microstructures were measured. These measurements will be correlated back to the quantitative calculation of localized solidification conditions. The distances were measured at ten different locations on the same weld track. The results from these measurements are summarized in Table 5. In this section, we will discuss only the results from two extreme conditions: from weld track 1 (Figure 3) made with 1 mm/s and weld track 7 (Figure 5) made with welding speed of 83 mm/s. The solidification velocity and thermal gradient were

calculated at these distances along the center of the weld track moving from WPB to the top of the weld, using Rosenthal model outlined in appendix 8.4. The measurements relevant to the eutectic transition focused only on the distance between WPB to the region at which the first observation of eutectic microstructure. The measurements ignored the complexity of the microstructures at the top and center of the weld track which may be affected by the weld pool curvature along the welding direction.

Table 5 Average distance from the WPB to the observed phase transition, as well as the calculated solidification velocity and thermal gradient range across the error.

Transition	Average Distance (μm)	Standard Deviation (μm)	Mapped Solidification Velocity (m/s)	Mapped Thermal Gradient (K/m)
$Al_{10}Mn_2Ce$ to $Al_{20}Mn_2Ce$	71.65	17.87	$6.77x10^{-4}$-$8.22x10^{-4}$	$4.14x10^{6}$-$4.15x10^{6}$
$Al_{20}Mn_2Ce$ to Eutectic	73.85	4.92	$5.89x10^{-2}$-$6.18x10^{-2}$	$5.23x10^{6}$-$5.29x10^{6}$

The model predictions for the solidification velocity and thermal gradients were used to calibrate the IRFs for primary solidification of $Al_{10}Mn_2Ce$ and $Al_{20}Mn_2Ce$. The calibration was performed by tuning the Gibbs-Tomson coefficients of the $Al_{10}Mn_2Ce$ and $Al_{20}Mn_2Ce$ ($1.14x10^{-6}$ and $1.57x10^{-6}$ m-k) respectively. The calibrations continued until the interface temperature for the primary phases was the same as that of the temperature isotherm at which the transition of $Al_{10}Mn_2Ce$ to $Al_{20}Mn_2Ce$ occurred. Similarly, calibrations continued until the interface temperature of $Al_{20}Mn_2Ce$ was the same as that of the isotherm at which eutectic microstructure was observed. The fitted Gibbs-Thomson coefficients are within the same order of magnitude as those previous used for Al-Cu and Al-Cu-1Si-1Fe systems ($1.08x10^{-6}$ m-k) [65,66]. Figure 8 shows the results of the fitted IRFs where the transitions between dominant solidification modes match with experimental observations.

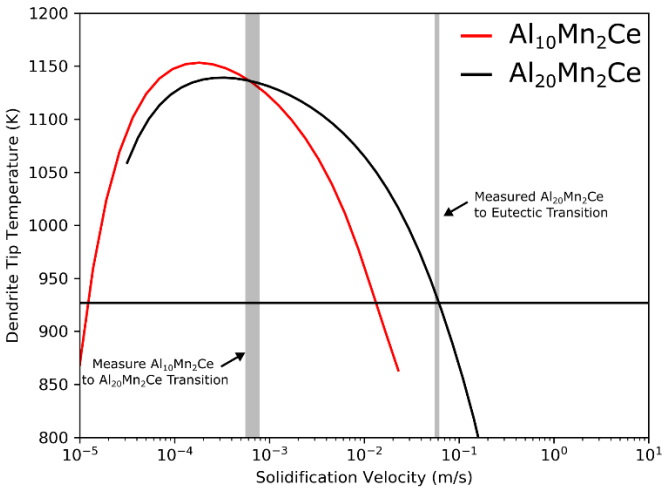

Figure 8 The undercooling predicted from the Dendritic IRF for $Al_{20}Mn_2Ce$ and $Al_{10}Mn_2Ce$ is shown for a Gibbs-Thomson Coefficient of $1.57x10^{-6}$ and $1.14x10^{-6}$ (m/k) respectively.

Our above mentioned IRF calculations for the Al-Ce-Mn system need to be compared against other calculations of solidification behaviors in the same alloy system. In previous research, Yang et al. [36] showed that the nucleation of the primary $Al_{20}Mn_2Ce$ phase was preferred over the primary $Al_{10}Mn_2Ce$ phase at low undercoolings. However, the model developed by Yang *et al.* did not consider the undercooling based on solidification conditions (solidification velocity, thermal gradient, and composition), thereby removing the link between processing and microstructure. Now that a relationship between solidification conditions and phase selection has been developed, it is possible to investigate additional compositions to provide insight into how the solidification pathways will change.

The effect of changing composition on the primary phase selection for the Al-Ce-Mn system was evaluated by varying both Ce and Mn between 0.5 and 6.5 at%. The dendritic IRF was calculated for each composition at set solidification velocities (10^{-4}, 10^{-2}, and 10^{-1} m/s) and thermal gradients (10^{6} K/m), and the selected phase was plotted over the given composition range in the Al-rich corner of the ternary system (Figure 9). The Al_6Mn and $Al_{11}Ce_3$ phases were neglected because they were not observed in our results. In Figure 9A, the liquidus projection of the Al-Ce-Mn system shows the location of the bulk composition with respect to the expected equilibrium phases. Figure 9B-C show the results of the dendritic IRF primary phase selection calculations for the given composition range and increasing solidification velocities. In Figure 9B, with the bulk composition, the calculations predicted primary $Al_{10}Mn_2Ce$ formation. With slight changes to the composition of our bulk material, we found that the results of our calculations are insensitive to the selected primary phase. However, if we change the solidification velocity to 10^{-2} (m/s), as shown in Figure 9C, the primary $Al_{10}Mn_2Ce$ is no longer the expected primary solidification phase. The benefit of such ability to predict the primary phase selection is that it allows for the tailoring of the as-built microstructure by choosing processing conditions. As expected, as the solidification velocity increased, the alloy favors the formation of metastable primary phases, eventually culminating in a eutectic between FCC Al and $Al_{20}Mn_2Ce$. Additionally, as the solidification velocity increases the length scale between phases decreases, which likely contribute to a variety of changes in hardness, as discussed in Section 5.3.

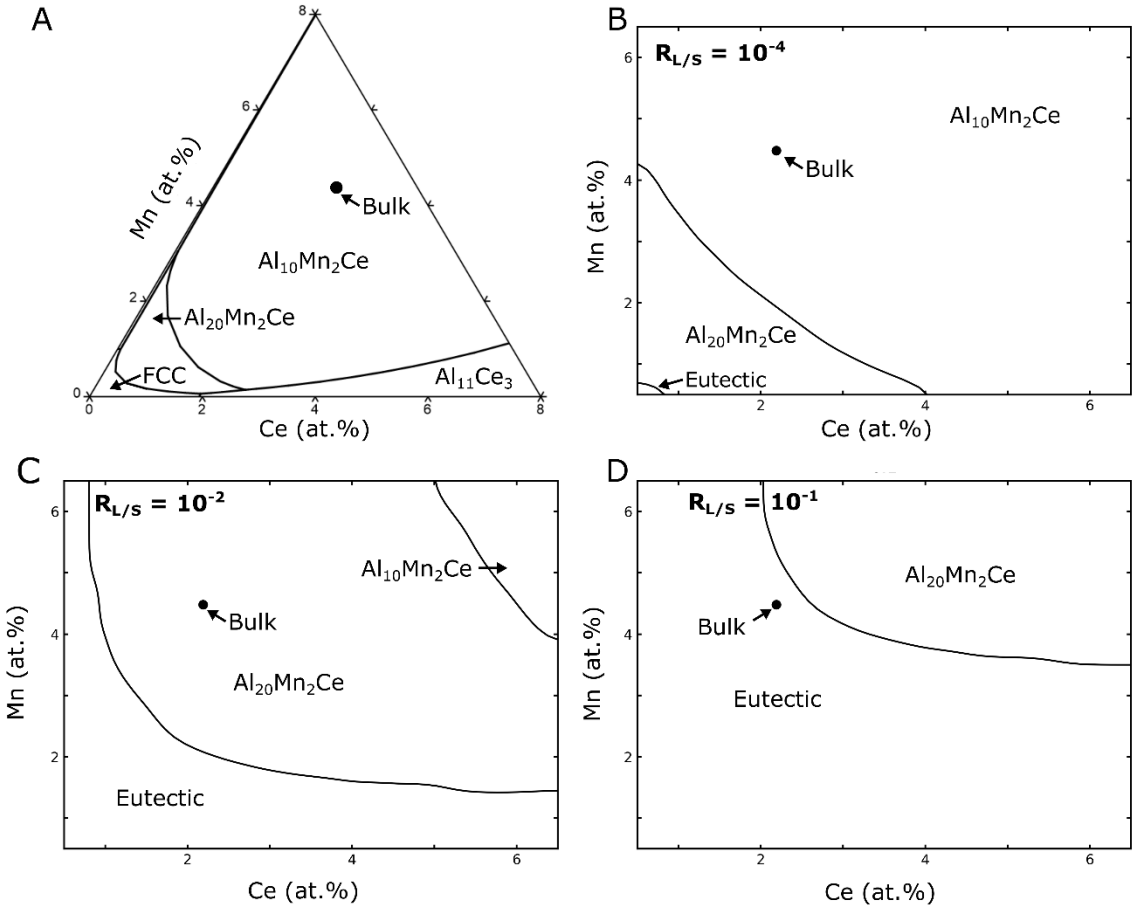

Figure 9 shows the (A) Liquidus projection of the Al-Ce-Mn system. (B) shows the expected solidification phase at a solidification velocity of $1x10^{-4}$ (m/s). (C) shows the expected solidification phase at a solidification velocity of $1x10^{-2}$ (m/s). (D) shows the expected solidification phase at a solidification velocity of $1x10^{-1}$ (m/s). The simulations have a set thermal gradient of $1x10^{6}$ (K/m)

5.2 Solid-State Decomposition

The solid-state decomposition of the Al-Ce-Mn weld tracks was found to be sensitive to the solidification microstructure. Figure 10 summarizes the observed decomposition pathways. Weld track 1 (Figure 3) contains two primary solidification phases, $Al_{10}Mn_2Ce$ and $Al_{20}Mn_2Ce$. The primary $Al_{10}Mn_2Ce$ phase (Figure 10A) did not decompose during heat treatment (Figure 10E). In contrast, the primary $Al_{20}Mn_2Ce$ (Figure 10B) decomposed into $Al_{11}Ce_3$ and an Al-Mn binary phases (Figure 10F), consistent with previous literature [32,37,51]. As the laser velocity increased in weld track 7 (Figure 5), the primary $Al_{10}Mn_2Ce$ was suppressed and the primary $Al_{20}Mn_2Ce$ and a eutectic between FCC Al and $Al_{20}Mn_2Ce$ was promoted. The primary $Al_{20}Mn_2Ce$ phase (Figure 10C) followed two decomposition pathways. Pathway 1 is where the $Al_{20}Mn_2Ce$ phase decomposed into the $Al_{11}Ce_3$ and Al-Mn binary phases similar to weld track 1 (bottom of Figure 10G). In pathway 2, the primary $Al_{20}Mn_2Ce$ phase decomposed into a plate

phase (top of Figure 10G). The plate phase is observed in all weld tracks except weld track 1 (Figure 3). The eutectic between FCC Al and $Al_{20}Mn_2Ce$ (Figure 10D) was observed to decompose plate phase (Figure 10H). The eutectic appears to have the same decomposition pathway that was observed in a previous work [51], where a similar plate morphology was identified as $Al_{51}Mn_7Ce_4$.

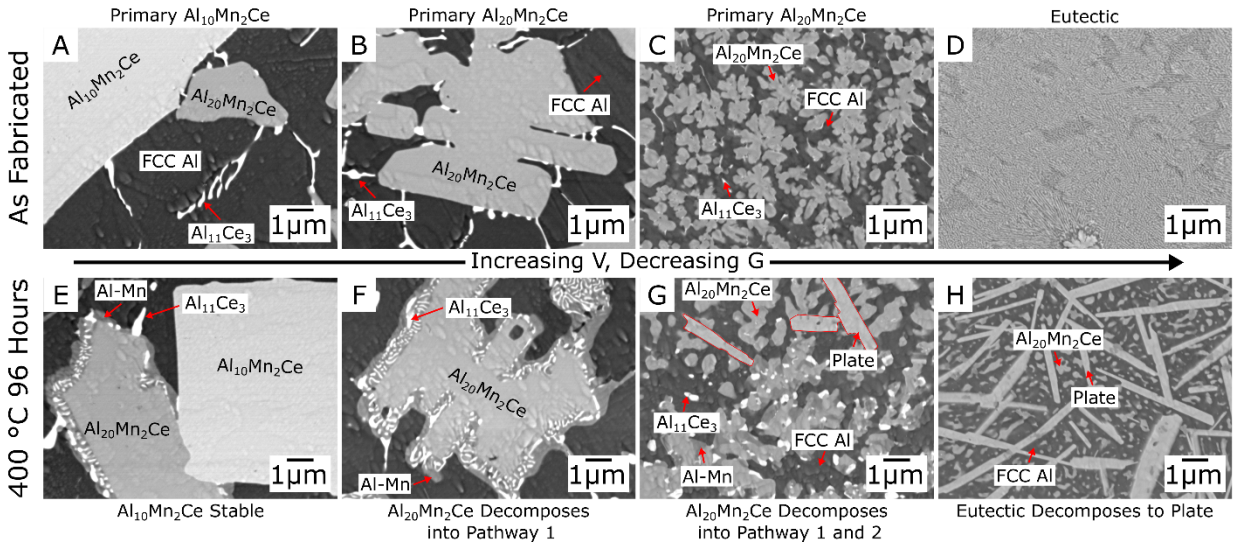

Figure 10 shows SEM BSE demonstrating the different phase selection and decomposition. (A) weld track 1 with primary $Al_{10}Mn_2Ce$ with small $Al_{20}Mn_2Ce$, $Al_{11}Ce_3$ and FCC Al. (B) weld track 1 with Primary $Al_{20}Mn_2Ce$ surrounded by FCC Al and $Al_{11}Ce_3$. (C) weld track 7 with Primary $Al_{20}Mn_2Ce$ surrounded by FCC Al and $Al_{11}Ce_3$. (D) weld track 7 with Eutectic between FCC Al and $Al_{20}Mn_2Ce$. (E) weld track 1 showing $Al_{10}Mn_2Ce$ stability. (F) weld track 1 showing $Al_{20}Mn_2Ce$ decomposing into $Al_{11}Ce_3$ and Al-Mn binary. (G) weld track 7 showing $Al_{20}Mn_2Ce$ decomposing into two different pathways: (1) $Al_{11}Ce_3$ + Al-Mn Binary, (2) plate phase. (H) weld track 7 eutectic decomposing into a plate phase.

In previous work [51], it was demonstrated that the change in phase selection during decomposition of the $Al_{20}Mn_2Ce$ phase was linked to the local composition of FCC Al and $Al_{20}Mn_2Ce$. This implies that the driving forces of the product phases are affected by the local composition, as well as possible orientation relationships of the parent phases, governing the nucleation of new phases. It is likely that the composition of FCC Al and $Al_{20}Mn_2Ce$ vary as the local solidification conditions change [67–69]. For example, in previous work [51], a key difference was the amount of Ce in the $Al_{20}Mn_2Ce$ phase which varies from 2.84 to 5.62 (at.%). It is shown in the manipulating of the bulk composition and solidification velocity results in changes in the primary phase selection. in summary, the local solidification condition influences the decomposition pathways of the primary phases at high temperature, and thereby the final microstructural distributions after heat treatment.

5.3 Implications of Modifying Solidification Microstructure

The implication of the primary phase selection, solid-state phase transformations, and microstructure refinement can be seen in Figure 11. Figure 11, shows the hardness of the 1, 10, and 83 mm/s weld tracks. The indent numbers start at the edge of the PMZ and the WPB (indent 1) and move inward to the top of the weld track (indent 7). The spacing between indents is changed to account for the difference in weld pool depth. The first observation is that as the laser velocity increased, the average hardness in

each weld track increased, as seen in Figure 11D. The increase is likely caused by the refinement in spacing between particles, which can be observed in Figure 3-5. The heat-treated hardness in weld track 1 and weld track 2 (Figure 11 A, B) retain similar hardness values after heat treatment. It is notable that hardness indents in both weld track 1 (Figure 3) and weld track 2 (Figure 4) was influenced by the primary $Al_{20}Mn_2Ce$ phase, except for indent 2 in weld track 1 which is primary $Al_{10}Mn_2Ce$, the softest region. In weld track 7 (Figure 5), the hardness-variation is large. In the primary $Al_{20}Mn_2Ce$ region sampled by indents 2-4, the hardness is similar before and after heat treatment. In the eutectic region, denoted by indent 5, the hardness is measured to a peak of 242 Vickers hardness value (VHV) in the as fabricated case. After heat treatment, the eutectic region decomposed, and the microstructure length scale increased to a similar size to other regions. The TWT (top of weld track) is the region that transitioned from eutectic back to primary $Al_{20}Mn_2Ce$, as mentioned before, likely caused by complex solidification conditions and showed softening. The increase in hardness values as a function of increasing laser velocity confirms the role of primary solidification of intermetallic phase in the Al-Ce-Mn system. These results point to the conclusion that locally tailorable hardness assuming that the solidification conditions can locally be controlled using the IRF models developed in this research.

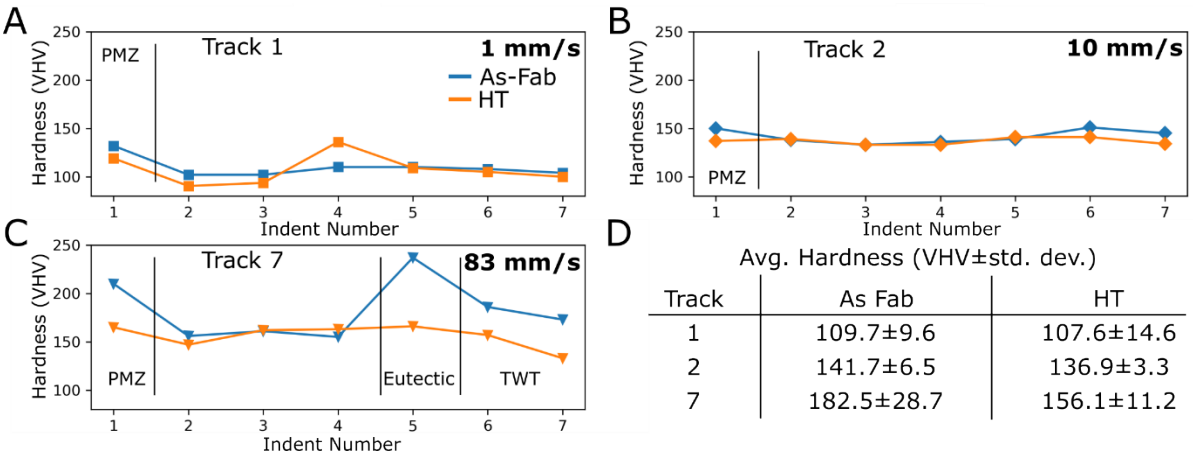

Figure 11 shows the hardness of three weld tracks in the as-fabricated and heat-treated cases. (A) shows weld track 1 (1 mm/s) where the hardness is largely consistent across the weld pool. (B) shows weld track 2 (10 mm/s) where the hardness is increased compared to weld track 1. (C) shows weld track 7 (83 mm/s) which demonstrates changes in hardness with different microstructure selection from primary $Al_{20}Mn_2Ce$ to eutectic. (D) shows the average hardness of each weld track with the standard deviation of the measured hardness.

6 Conclusions

The solidification phase selection of an Al-10Ce-8Mn (wt.%) alloy was examined by varying the velocity of laser tracks over an AM substrate with the same composition. The results revealed three solidification regions: primary $Al_{10}Mn_2Ce$, primary $Al_{20}Mn_2Ce$, and a eutectic between FCC Al and $Al_{20}Mn_2Ce$. In the experiments, the primary $Al_{10}Mn_2Ce$ was calculated to form at solidification velocities below $7.79x10^{-4}$ (m/s) and was suppressed with more rapid solidification conditions. The formation of primary $Al_{20}Mn_2Ce$ was calculated to occur at a solidification velocity between $5.84x10^{-4}$ and $7.79x10^{-4}$ (m/s) and with thermal gradient range of $4.56x10^{6}$ to $4.57x10^{6}$ (K/m) . The primary $Al_{20}Mn_2Ce$ was suppressed, and the

formation of a eutectic microstructure was promoted at a solidification velocity above $5.69x10^{-2}$-$6.01x10^{-2}$ (m/s) and thermal gradient of $5.16x10^{6}$-$5.22x10^{6}$ (K/m).

Previously published dendritic interface response function models, based on a linearized liquidus slope, were unable to describe the experimentally observed phase selection even with fitting. Therefore, the interface response function model was extended for non-linear slopes calculated with direct interface to a comprehensive thermodynamic model. With this modified approach and by fitting the Gibbs-Thomson coefficients to observations in solidification microstructure selection, the modified IRF model was able to describe the experimentally observed phase selection.

The solid-state decomposition pathways for the Al-Ce-Mn weld tracks were evaluated and compared with published results. The primary $Al_{10}Mn_2Ce$ did not decompose due to its higher stability compared to other potential phases. The primary $Al_{20}Mn_2Ce$ followed two different decomposition pathways. First, the primary $Al_{20}Mn_2Ce$ phase decomposed into $Al_{11}Ce_3$ and an Al-Mn binary phase. Second, the primary $Al_{20}Mn_2Ce$ decomposed into a plate phase. Similarly, the eutectic microstructure containing the FCC Al and $Al_{20}Mn_2Ce$ phases decomposed into a plate phase.

7 Acknowledgements

This manuscript has been authored by UT-Battelle, LLC, under contract DE-AC05-00OR22725 with the US Department of Energy (DOE). The US government retains and the publisher, by accepting the article for publication, acknowledges that the US government retains a nonexclusive, paid-up, irrevocable, worldwide license to publish or reproduce the published form of this manuscript, or allow others to do so, for US government purposes. DOE will provide public access to these results of federally sponsored research in accordance with the DOE Public Access Plan (http://energy.gov/downloads/doe-public-access-plan).

This research was cosponsored by the DOE Office of Energy Efficiency and Renewable Energy, Vehicle Technologies Office, Powertrain Materials Core Program and by the DOE Advanced Materials and Manufacturing Technologies Office Manufacturing Demonstration Facility at ORNL.

8 Appendix

8.1 EBSD Phase Identification for the 1 mm/s weld track

EBSD was used to locally identify phases in weld track 1. The results of the EBSD mapping are seen in Figure A1. The EBSD was collected on a Bruker detector using a Ziess Gemni 450. The EBSD patterns collected are all within the expected range for positive identification provided by Bruker. The specified range is that the N value (the number of identified bands) is at least seven out of twelve and the band mismatch value (BMM) is below 1.7°, as described in the Bruker EBSD manual.

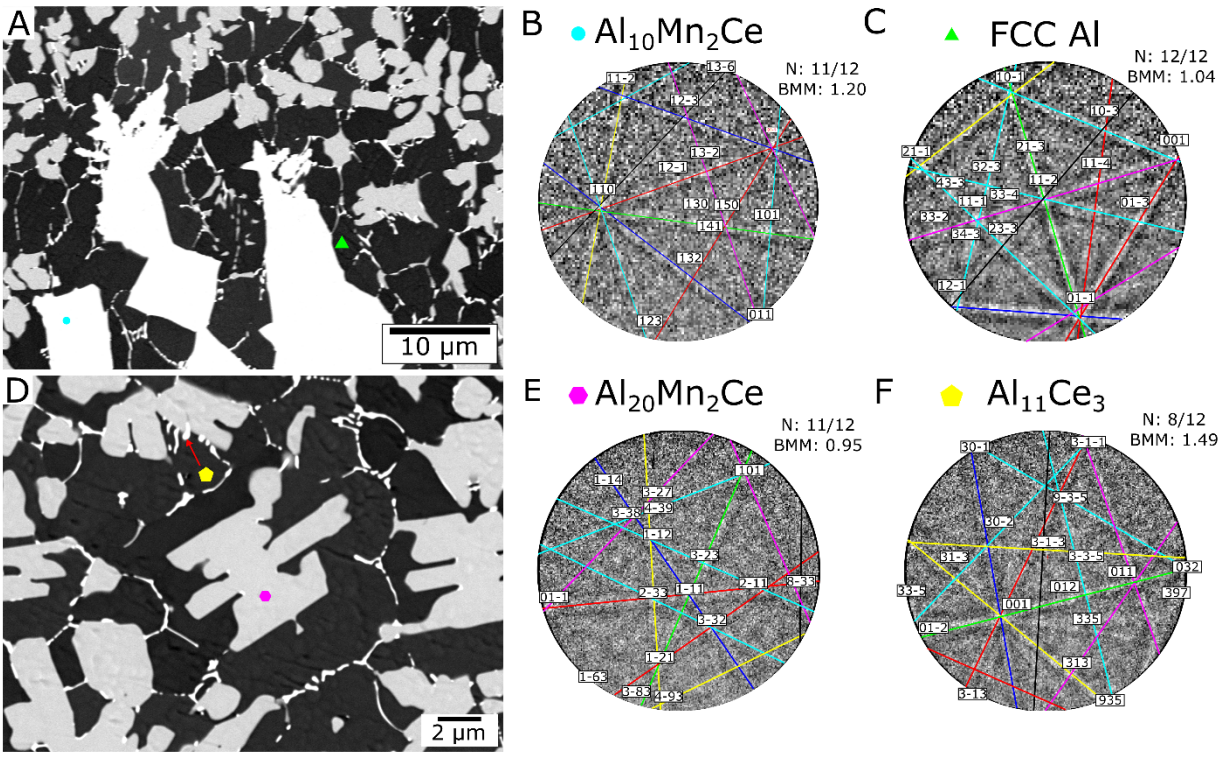

Figure A1 shows the EBSD patterns correlated to localized phase selection, where (A) is an overview of the region where the $Al_{10}Mn_2Ce$ (B) and FCC Al (C). (D) shows the locations for the EBSD patterns of $Al_{20}Mn_2Ce$ (E) and $Al_{11}Ce_3$ (F).

8.2 Linear Interface Response Function Approximation

The goal of this section is to expand of the linear interface response described for Eq. (1). Therefore, we must first describe the equations that make up the total undercooling the system. The first term, ΔT_R, is an undercooling resulting from the capillary effect and is described in the following equation.

$$\Delta T_R = \frac{2\Gamma}{R}$$	*(3)*

Where R is the dendrite tip radius, and Γ is the Gibbs Thomson coefficient described by,

$$\Gamma = \frac{\gamma V_m}{\Delta S_m}$$	*(4)*

where γ is the interfacial energy between the solid and the liquid phases, V_m is the molar volume of the phase, and ΔS_m is the entropy of fusion per mole for the solid phase forming from the liquid. The

capillary effect is simply a result of the predicted radius and does not influence the iterative solution on the system. The cellular undercooling at low interface velocities is defined by,

$$\Delta T_{Cell} = \frac{GD}{V}$$	*(5)*

where G is the thermal gradient, V is the solidification velocity, and D is the liquid diffusivity of the solute. The ΔT_k undercooling has been described by Kurz et al. [52] for a dilute linear system with the equation.

$$\Delta \mathrm{T_k} = \frac{V m_i}{V_0\left(1 - k_0^i\right)}$$	*(6)*

where, m_i is the liquidus slope for each element i, V_0 is on the order of the velocity of sound in a solid solution matrix. For intermetallic compounds, V_0 is controlled by bulk liquid diffusion [70], D_l and speed of interface diffusion, V_{DI}. V is the input solidification velocity, and k_0^i is the equilibrium partition coefficient for the element of interest (i = Ce, Mn).

The next undercooling terms, ΔT_C, has been previously derived by Kurz and Trivedi [52] for an assumed linear phase diagram. In the derivation of the IRF by Kurz and Trivedi, the Ivantsov [71] solution is used to describe concentration profile across a parabolic dendrite tip, assuming both the diffusion and shape preservation equations are satisfied [52]. The Ivantsov solution describes the tip of a dendrite by defining it as a fixed shape parabola for a set solutal Peclet number growing into the liquid at a steady state. The Peclet number describes the transport of a substance by bulk motion of a fluid (advection) to the rate of the diffusion transport. The differential equation governing the steady state solute diffusion is defined by,

$$\frac{\partial^2 C}{\partial z^2} + \left(\frac{V}{D}\right)\left(\frac{\partial C}{\partial z}\right) = 0$$	*(7)*

where C is concentration, V is the solidification velocity, D is solute diffusivity in the liquid, and z is the distance away from the dendrite tip. To solve the steady state solute diffusion relationship, Ivantsov derived a coordinate transformation from a parabolic axis to determine the composition of the liquid at a dendrite tip. The solution to Eq. (7) is shown in Eq. *(8)*.

$$C_{t,i} = \frac{C_{0,i}}{1 - \left(1 - k_0^i\right) Iv(Pe_i)}$$	*(8)*

where $\mathrm{C_{t,i}}$ is the composition in the liquid at the dendrite tip (for each element, i), $\mathrm{C_{0.i}}$ is the bulk composition of the liquid (for each element, i), k_0^i is the equilibrium partition coefficient. (for each element, i), and Pe_i is the Peclet number (for each element, i), which is a dimensionless number defined by Eq. *(9)*.

$$Pe_i = \frac{RV}{2D_i}$$	*(9)*

where R is the dendrite tip radius, V is the solidification velocity, and D_i is the liquid diffusivity of element i. *Iv* is the Ivantsov function defined for a parabolic geometry is defined by,

$$Iv(Pe_i) = Pe_i * e^{Pe_i} * E_1(Pe_i)$$	*(10)*

Where $E_1(Pe)$ is the exponential integral function of the Peclet number. In the current application, the solidification velocity (V) and thermal gradient (G) are fixed, and an iterative solution is used for determining the radius, which subsequently determines the Peclet number. The radius solution used is estimated from the linear stability analysis of a planar front [50], defined by,

$$R = \left(\frac{\Gamma}{\sigma^*(\sum_0^i m_i G_{c,i}\xi_i - G)}\right)^{\frac{1}{2}}$$	*(11)*

where, σ^* is the dendrite tip selection parameter determined by Kurz and Trivedi as 0.025 [52], m_i is the liquidus slope (for each element, i), for the linear approximation, the liquidus slope is defined at the initial liquidus composition, *G* is the thermal gradient of the material into the solid, ξ_i is the deviation from equilibrium also known as the variation for solute as a function of the Peclet number (for each element, i), defined by,

$$\xi_i = \frac{2k_0^i}{\sqrt{1 + \frac{1}{Pe_i^2\sigma^*}} - 1 + 2k_0^i}$$	*(12)*

and $G_{c,i}$ is the concentration gradient in the liquid ahead of the dendrite tip for each element i,

$$G_{C,i} = \frac{(C_{t,i} - C_{0,i})V}{D_i\, Iv(Pe_d)}$$	*(13)*

These equations are used by Kurz and Trivedi as well as other authors [52,72]. Once a solution is found that converges on a dendrite tip radius, the undercooling of the system can be determined. In the current example, the solution is defined by the linear approximation from Kurz and Trivedi [52]. The linear approximation defines the liquidus line using the equation $T_t = T_M + mC_t$, where T_t is the dendrite tip temperature, T_m is the pure melt temperature, m is the linear liquidus slope, and C_t is the

composition of the liquid at the dendrite tip interface. Using the direct example given by Kurz and Trivedi, the undercooling of a dendrite tip is defined by,

$$\Delta T_{undercooling} = \sum_i \left(\frac{k_0^i \Delta T_0 Iv(Pe_i)}{1-(1-k_0^i)Iv(Pe_i)} + \frac{Vm_i}{V_0(1-k_0^i)} \right) + \frac{2\Gamma}{R} + \frac{GD}{V} \quad (14)$$

Where the ΔT_C term is replaced as a function of linear approximation described by Kurz *et al.* [52]. Using the solution to undercooling, the dendrite tip temperature can be calculated using the relationship,

$$T_{Dendrite} = T_{liquid} - \Delta T_{undercooling} \quad (15)$$

Where T_{liquid} is the liquidus temperature of the phase of interest at the bulk composition, and Δ $T_{Dendrite}$ is the dendrite tip temperature.

The initial derivation shown above assumes that there is no deviation from thermodynamic equilibrium between liquid and solid phases. However, it is well understood that during solidification non-equilibrium effects occur. Kurz and Trivedi acknowledge three non-equilibrium effects (1) the effect of attachment kinetics, (2) the variation in solute partitioning as a function of velocity, and (3) the change in interface compositions due to thermodynamic constraints. The three non-equilibrium effects will play a role together to determine a non-equilibrium composition of the liquid at the dendrite tip and dendrite tip. However, the deviation to a non-equilibrium state will not be explored in the current work because of the fixed composition of the intermetallic compounds of interest in the CALPHAD description provided by Yang *et al.* [36]. The fixed composition removes the ability to effectively model the phase descriptions with Aziz's solute trapping model [68] because the solid composition is fixed. More information about the non-equilibrium solidification can be found by a variety of authors [52,67,73].

To evaluate this linearized phase diagram assumption, it will be initially applied to the Al-Ce-Mn system. The values used for this calculation are shown in Table 2. The diffusivity of Ce in liquid aluminum is not well described in literature and is assumed at 2.5×10^{-9} m^2/s. For a comparison of the primary solidification undercooling to the undercooling in the eutectic, a constant eutectic temperature (at 927 K), determined by PANDAT for the bulk composition (Al-10Ce-8Mn (wt.%)), was adopted to approximate the expected transition point.

Using these values, the dendritic IRF was calculated as shown in Figure A2 for a linearized phase diagram. Figure A2 A shows the dendritic tip temperature calculated for all three phases, i.e., FCC Al, $Al_{10}Mn_2Ce$ and $Al_{20}Mn_2Ce$. The $Al_{20}Mn_2Ce$ phase was assumed to have a Gibbs-Thomson Coefficient of 1.35×10^{-7} (m-K) and the dendrite tip temperature vs. solidification velocity was calculated at a given thermal gradient. The calculated transition from the preferential growth of primary $Al_{10}Mn_2Ce$ to the preferential growth of primary $Al_{20}Mn_2Ce$ occurred at a solidification velocity of ~1.38×10^{-3} (m/s). Based on the experimental results, the transition between primary $Al_{10}Mn_2Ce$ and primary $Al_{20}Mn_2Ce$ is expected to occur between solidification velocities 5.84×10^{-4} and 7.79×10^{-4} (m/s). In addition, the undercooling of the primary $Al_{20}Mn_2Ce$ phase never decreases below the expected eutectic temperature at 927 K. This implies that the IRF model is able to predict the phase selection of $Al_{20}Mn_2Ce$ above the 1.38×10^{-3} (m/s) liquid-solid interface velocity, until the calculation becomes unstable. It is well known that this critical velocity leading to unstable calculation corresponds to the transition from dendrite to planar growth. However, this result does not agree with our experimental result, where the primary $Al_{20}Mn_2Ce$ is observed to transition to eutectic solidification between 5.69×10^{-2} and 6.01×10^{-2} (m/s), with

similar thermal gradient. Therefore, in attempt to fit the model to the experimental results, the Gibbs-Thomson Coefficient was increased to $1x10^{-5}$ (m-K). This is indeed an unreasonable value for the Gibbs-Thomson coefficient. The result (see Figure A2 B) does increase the undercooling of the system, but it no longer predicts a transition from primary $Al_{10}Mn_2Ce$ to primary $Al_{20}Mn_2Ce$. Furthermore, it does not predict eutectic solidification. Therefore, in this work we focused on eliminating the assumption of the linearized liquidus slope with direct calculation of the non-linear liquidus slope from thermodynamic models.

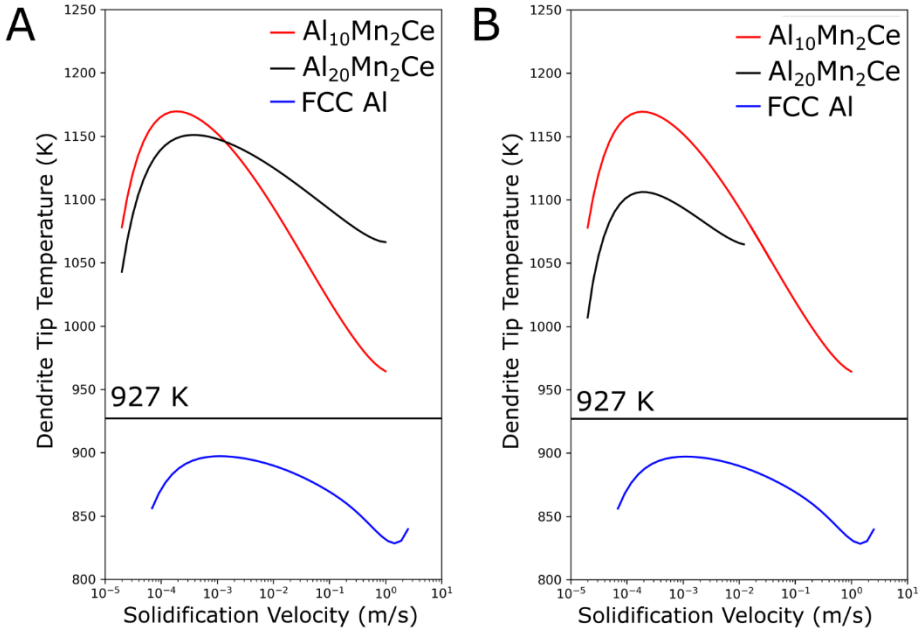

Figure A2 The undercooling predicted from the Dendritic IRF for FCC Al, $Al_{20}Mn_2Ce$ and $Al_{10}Mn_2Ce$ is shown in (A) for a Gibbs-Thomson Coefficient of $Al_{20}Mn_2Ce$ of $1.35x10^{-7}$(m/k) that does not match the experimental results in Section 4.2. In (B) the Gibbs-Thomson Coefficient is increased to $1x10^{-5}$ (m/k) to attempt to fit the system to the experimental results, however it is still unable to match experimental results.

8.3 Non-linear implementation

In order to couple the IRF with CALPHAD software, it is important to have a workflow that minimizes the interactions with the external calculation because the computational time is the most expensive. To attempt to ease the burden, a template for the calculation of the undercooling of intermetallic phases is provided in Figure A3. The layout only calculates the thermodynamic equilibrium once per iteration with fixed composition intermetallic compounds. It should be noted that if solute trapping is implemented using attachment kinetics described by Trivedi et al. [52], the solution because more expensive as the partition coefficients must be solved iteratively allowing for a driving force for the liquid to transform to solid.

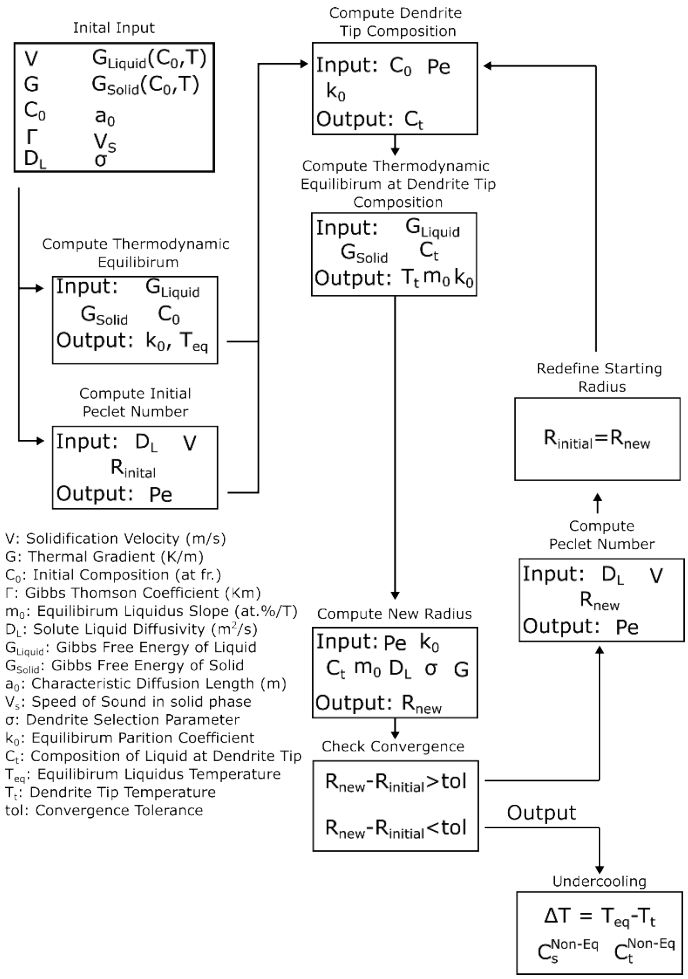

Figure A3 Layout of solution to IRF Model.

The reason for implementing the direct calculation of the phase diagram for the dendritic IRF are linked to the rapid increase in partition coefficient and liquidus slope as a function of the dendrite tip composition. In Figure A4, the dendrite tip composition, liquidus slopes, and partition coefficients of Ce and Mn as a function of solidification velocity are plotted for the context. In the figure, it is notable as the velocity increases, the rate at which the liquidus slope and partition coefficients change increases causing the undercooling to decrease rapidly.

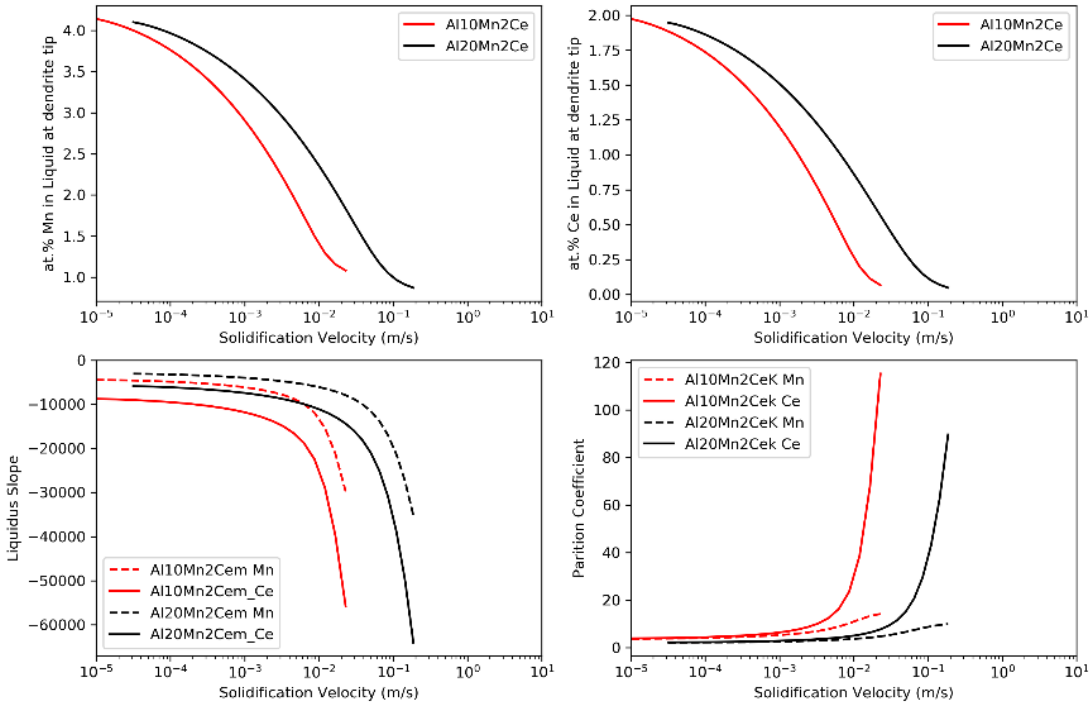

Figure A4 (A) at.% Mn in liquid at dendrite tip. (B) at.% Ce in liquid at dendrite tip, (C) Liquidus Slope, (D) partition coefficient.

8.4 Rosenthal Model

To model the thermal conditions in the weld tracks, i.e., liquid/solid interface velocity, thermal gradient and subsequent cooling conditions, the Rosenthal model [54,60] was used. It is well known that this model is only applicable for point heat source and a plate geometry with infinite dimensions. The model assumes conduction is the only heat transfer mechanism and ignores the radiation and convection, in response to a heat source moving along the x-axis with constant velocity, v. In the current case v is a vector represented by the $\vec{v} = [v, 0, 0]$. The temperature at a given point is described by,

$$T(x,y,z) = T_0 + \frac{\eta P}{2\pi k}\left(\frac{1}{R}\right)\exp\left(-\frac{v}{2a}(R+x)\right), \quad (16)$$

where, T_0 is the initial temperature of the substrate, η is the laser absorption efficiency of the material, P is the input power, k is the thermal conductivity, α is the thermal diffusivity. The distance to the heat source, R, is.

$$R = \sqrt{x^2 + y^2 + z^2}, \quad (17)$$

where, x, y, and z coordinates relative to the heat source. The magnitude of the thermal gradient at the liquid/solid interface was determined by the derivative at the temperature isotherm of interest, described by

$$G = \left| \sqrt{\left(\frac{\partial T}{\partial x}\right)^2 + \left(\frac{\partial T}{\partial y}\right)^2 + \left(\frac{\partial T}{\partial z}\right)^2} \right|_{T=T_L} \quad (18)$$

where T_L is the liquidus temperature. Using the thermal gradient, the solidification velocity is determined through a geometric relationship with the laser trajectory [53,74],

$$V_s = \vec{v} \cdot \vec{n} \quad (19)$$

where V_s is the solidification velocity, $\vec{v}$ is the direction of the laser, and $\vec{n}$ is the unit vector normal to the weld track surface determined by the thermal gradient. It is important to note that in the Rosenthal model, the steady-state solidification velocity is limited to the laser velocity, as the maximum surface normal is one.

9 References

[1] W.J. Sames, F.A. List, S. Pannala, R.R. Dehoff, S.S. Babu, The metallurgy and processing science of metal additive manufacturing, Int. Mater. Rev. 61 (2016) 315–360. https://doi.org/10.1080/09506608.2015.1116649.

[2] R.R. Dehoff, M. Kirka, W.J. Sames, H. Bilheux, A.S. Tremsin, L.E. Lowe, S.S. Babu, Site specific control of crystallographic grain orientation through electron beam additive manufacturing, Mater. Sci. Technol. (United Kingdom). 31 (2015). https://doi.org/10.1179/1743284714Y.0000000734.

[3] M. Haines, A. Plotkowski, C.L. Frederick, E.J. Schwalbach, S.S. Babu, A sensitivity analysis of the columnar-to-equiaxed transition for Ni-based superalloys in electron beam additive manufacturing, Comput. Mater. Sci. 155 (2018) 340–349. https://doi.org/10.1016/j.commatsci.2018.08.064.

[4] A. Plotkowski, J. Ferguson, B. Stump, W. Halsey, V. Paquit, C. Joslin, S.S. Babu, A. Marquez Rossy, M.M. Kirka, R.R. Dehoff, A stochastic scan strategy for grain structure control in complex geometries using electron beam powder bed fusion, Addit. Manuf. 46 (2021) 102092. https://doi.org/10.1016/j.addma.2021.102092.

[5] R.R. Dehoff, M.M. Kirka, F.A. List, K.A. Unocic, W.J. Sames, Crystallographic texture engineering through novel melt strategies via electron beam melting: Inconel 718, Mater. Sci. Technol. (United Kingdom). 31 (2015) 939–944. https://doi.org/10.1179/1743284714Y.0000000697.

[6] N. Raghavan, R. Dehoff, S. Pannala, S. Simunovic, M. Kirka, J. Turner, N. Carlson, S.S. Babu, Numerical modeling of heat-transfer and the influence of process parameters on tailoring the grain morphology of IN718 in electron beam additive manufacturing, Acta Mater. 112 (2016). https://doi.org/10.1016/j.actamat.2016.03.063.

[7] N. Raghavan, S. Simunovic, R. Dehoff, A. Plotkowski, J. Turner, M. Kirka, S. Babu, Localized melt-scan strategy for site specific control of grain size and primary dendrite arm spacing in electron beam additive manufacturing, Acta Mater. 140 (2017) 375–387. https://doi.org/10.1016/j.actamat.2017.08.038.

[8] N. Kaufmann, M. Imran, T.M. Wischeropp, C. Emmelmann, S. Siddique, F. Walther, Influence of process parameters on the quality of aluminium alloy en AW 7075 using Selective Laser Melting (SLM), Phys. Procedia. 83 (2016) 918–926. https://doi.org/10.1016/j.phpro.2016.08.096.

[9] R.A. Michi, A. Plotkowski, A. Shyam, R.R. Dehoff, S.S. Babu, Towards high-temperature applications of aluminium alloys enabled by additive manufacturing, Int. Mater. Rev. (2021). https://doi.org/10.1080/09506608.2021.1951580.

[10] A.B. Spierings, K. Dawson, T. Heeling, P.J. Uggowitzer, R. Schäublin, F. Palm, K. Wegener, Microstructural features of Sc- and Zr-modified Al-Mg alloys processed by selective laser melting, Mater. Des. 115 (2017) 52–63. https://doi.org/10.1016/j.matdes.2016.11.040.

[11] A.B. Spierings, K. Dawson, P. Dumitraschkewitz, S. Pogatscher, K. Wegener, Microstructure characterization of SLM-processed Al-Mg-Sc-Zr alloy in the heat treated and HIPed condition, Addit. Manuf. 20 (2018) 173–181. https://doi.org/10.1016/j.addma.2017.12.011.

[12] W.E. Frazier, Metal additive manufacturing: A review, J. Mater. Eng. Perform. 23 (2014) 1917–1928. https://doi.org/10.1007/s11665-014-0958-z.

[13] J.J. Lewandowski, M. Seifi, Metal Additive Manufacturing: A Review of Mechanical Properties, Annu. Rev. Mater. Res. 46 (2016) 151–186. https://doi.org/10.1146/annurev-matsci-070115-032024.

[14] E. Atzeni, A. Salmi, Study on unsupported overhangs of AlSi10Mg parts processed by Direct Metal Laser Sintering (DMLS), J. Manuf. Process. 20 (2015) 500–506. https://doi.org/10.1016/j.jmapro.2015.04.004.

[15] S. Romano, A. Brückner-Foit, A. Brandão, J. Gumpinger, T. Ghidini, S. Beretta, Fatigue properties of AlSi10Mg obtained by additive manufacturing: Defect-based modelling and prediction of fatigue strength, Eng. Fract. Mech. 187 (2018) 165–189. https://doi.org/10.1016/j.engfracmech.2017.11.002.

[16] N.T. Aboulkhair, N.M. Everitt, I. Ashcroft, C. Tuck, Reducing porosity in AlSi10Mg parts processed by selective laser melting, Addit. Manuf. 1 (2014) 77–86. https://doi.org/10.1016/j.addma.2014.08.001.

[17] N. Takata, H. Kodaira, K. Sekizawa, A. Suzuki, M. Kobashi, Change in microstructure of selectively laser melted AlSi10Mg alloy with heat treatments, Mater. Sci. Eng. A. 704 (2017) 218–228. https://doi.org/10.1016/j.msea.2017.08.029.

[18] A. Mauduit, S. Pillot, H. Gransac, Study of the suitability of aluminum alloys for additive manufacturing by laser powder-bed fusion, UPB Sci. Bull. Ser. B Chem. Mater. Sci. 79 (2017) 219–238.

[19] S.C. Alt, V.A. Yardley, Z. Shi, J. Lin, Challenges in additive manufacturing of high-strength aluminium alloys and current developments in hybrid additive manufacturing, 4 (2021). https://doi.org/10.1016/j.ijlmm.2020.12.004.

[20] J. Liu, P. Wen, Metal vaporization and its influence during laser powder bed fusion process, Mater. Des. 215 (2022). https://www.sciencedirect.com/science/article/pii/S0264127522001265?via%3Dihub#ab010.

[21] D. Weiss, Improved High-Temperature Aluminum Alloys Containing Cerium, J. Mater. Eng. Perform. 28 (2019) 1903–1908. https://doi.org/10.1007/s11665-019-3884-2.

[22] Y. Liu, R.A. Michi, D.C. Dunand, Cast near-eutectic Al-12.5 wt.% Ce alloy with high coarsening and creep resistance, Mater. Sci. Eng. A. 767 (2019) 138440. https://doi.org/10.1016/j.msea.2019.138440.

[23] A. Plotkowski, O. Rios, N. Sridharan, Z. Sims, K. Unocic, R.T. Ott, R.R. Dehoff, S.S. Babu, Evaluation of an Al-Ce alloy for laser additive manufacturing, Acta Mater. 126 (2017) 507–519. https://doi.org/10.1016/j.actamat.2016.12.065.

[24] H.B. Henderson, J.A. Hammons, A.A. Baker, S.K. McCall, T.T. Li, A. Perron, Z.C. Sims, R.T. Ott, F. Meng, M.J. Thompson, D. Weiss, O. Rios, Enhanced thermal coarsening resistance in a nanostructured aluminum-cerium alloy produced by additive manufacturing, Mater. Des. 209 (2021) 109988. https://doi.org/10.1016/j.matdes.2021.109988.

[25] E.T. Stromme, H.B. Henderson, Z.C. Sims, M.S. Kesler, D. Weiss, R.T. Ott, F. Meng, S.A.M. Kassoumeh, J. Evangelista, G. Begley, O. Rios, Ageless Aluminum-Cerium-Based Alloys in High-Volume Die Casting for Improved Energy Efficiency, JOM. (2018). https://doi.org/10.1007/s11837-018-2861-9.

[26] L. Zhou, T. Huynh, S. Park, H. Hyer, A. Mehta, S. Song, Y. Bai, B. McWilliams, K. Cho, Y. Sohn, Laser powder bed fusion of Al–10 wt% Ce alloys: microstructure and tensile property, J. Mater. Sci. 55 (2020) 14611–14625. https://doi.org/10.1007/s10853-020-05037-z.

[27] A. Shyam, A. Plotkowski, S. Bahl, K. Sisco, L.F. Allard, Y. Yang, J.A. Haynes, R.R. Dehoff, An additively manufactured AlCuMnZr alloy microstructure and tensile mechanical properties, Materialia. 12 (2020). https://doi.org/10.1016/j.mtla.2020.100758.

[28] X. Hu, S. Bahl, A. Shyam, A. Plotkowski, B. Milligan, L. Allard, J.A. Haynes, Y. Ren, A. Chuang, Repurposing the θ (Al2Cu) phase to simultaneously increase the strength and ductility of an additively manufactured Al–Cu alloy, Mater. Sci. Eng. A. 850 (2022) 143511. https://doi.org/10.1016/j.msea.2022.143511.

[29] S. Bahl, K. Sisco, Y. Yang, F. Theska, S. Primig, L.F. Allard, R.A. Michi, C. Fancher, B. Stump, R. Dehoff, A. Shyam, A. Plotkowski, Al-Cu-Ce(-Zr) alloys with an exceptional combination of additive processability and mechanical properties, Addit. Manuf. 48 (2021) 102404. https://doi.org/10.1016/j.addma.2021.102404.

[30] K. Sisco, A. Plotkowski, Y. Yang, D. Leonard, B. Stump, P. Nandwana, R.R. Dehoff, S.S. Babu, Microstructure and properties of additively manufactured Al–Ce–Mg alloys, Sci. Rep. 11 (2021) 1–14. https://doi.org/10.1038/s41598-021-86370-4.

[31] R.A. Michi, K. Sisco, S. Bahl, Y. Yang, J.D. Poplawsky, L.F. Allard, R.R. Dehoff, A. Plotkowski, A. Shyam, A creep-resistant additively manufactured Al-Ce-Ni-Mn alloy, Acta Mater. 227 (2022) 117699. https://doi.org/10.1016/j.actamat.2022.117699.

[32] A. Plotkowski, K. Sisco, S. Bahl, A. Shyam, Y. Yang, L. Allard, P. Nandwana, A.M. Rossy, R.R. Dehoff, Microstructure and properties of a high temperature Al–Ce–Mn alloy produced by

additive manufacturing, Acta Mater. 196 (2020). https://doi.org/10.1016/j.actamat.2020.07.014.

[33] F. Theska, Y. Yang, K.D. Sisco, A. Plotkowski, S. Primig, On the high-temperature stability of the Al8Cu3Ce intermetallic in an additively manufactured Al-Cu-Ce-Zr alloy, Mater. Charact. 191 (2022) 112109. https://doi.org/10.1016/j.matchar.2022.112109.

[34] A. Perrin, S. Bahl, D.N. Leonard, R. Michi, K. Sisco, A. Plotkowski, A. Shyam, R. Dehoff, D. Shin, Y. Yang, Phase stability in cast and additively manufactured Al-rich Al-Cu-Ce alloys, J. Alloys Compd. 926 (2022) 166984. https://doi.org/10.1016/j.jallcom.2022.166984.

[35] S. Bahl, A. Plotkowski, T.R. Watkins, R.A. Michi, B. Stump, D.N. Leonard, J.D. Poplawsky, R. Dehoff, A. Shyam, M. Science, D. Oak, R. National, O. Ridge, 3D Printed eutectic aluminum alloy has facility for site-specific properties ☆, Addit. Manuf. 70 (2023) 103551. https://doi.org/10.1016/j.addma.2023.103551.

[36] Y. Yang, S. Bahl, K. Sisco, M. Lance, D. Shin, A. Shyam, A. Plotkowski, R.R. Dehoff, Primary solidification of ternary compounds in Al-rich Al–Ce–Mn alloys, J. Alloys Compd. 844 (2020) 156048. https://doi.org/10.1016/j.jallcom.2020.156048.

[37] M.A. Gordillo, I. Cernatescu, T.T. Aindow, T.J. Watson, M. Aindow, Phase stability in a powder-processed Al–Mn–Ce alloy, J. Mater. Sci. 49 (2014) 3742–3754. https://doi.org/10.1007/s10853-014-8086-6.

[38] B. Zheng, Y. Lin, Y. Zhou, E.J. Lavernia, Gas Atomization of Amorphous Aluminum : Part I . Thermal Behavior Calculations, (2009). https://doi.org/10.1007/s11663-009-9276-5.

[39] B. Zheng, Y. Lin, Y. Zhou, E.J. Lavernia, Gas Atomization of Amorphous Aluminum Powder : Part II . Experimental Investigation, 40 (2024) 995–1004. https://doi.org/10.1007/s11663-009-9277-4.

[40] S.C. Gill, W. Kurz, Rapidly solidified AlCu alloys-II. Calculation of the microstructure selection map, Acta Metall. Mater. 43 (1995) 139–151. https://doi.org/10.1016/0956-7151(95)90269-4.

[41] S.C. Gill, W. Kurz, Rapidly solidified AlCu alloys-I. experimental determination of the microstructure selection map, Acta Metall. Mater. 41 (1993) 3563–3573. https://doi.org/10.1016/0956-7151(93)90237-M.

[42] S. Fukumoto, W. Kurz, The delta to gamma transition in Fe-Cr-Ni Alloys during laser treatemtent, ISIJ Int. 37 (1997) 677–684.

[43] S. Fukumoto, W. Kurz, Solidification phase and microstructure selection maps for Fe-Cr-Ni alloys, ISIJ Int. 39 (1999) 1270–1279. https://doi.org/10.2355/isijinternational.39.1270.

[44] S.S. Babu, J.W. Elmer, J.M. Vitek, S.A. David, Time-resolved X-ray diffraction investigation of primary weld solidification in Fe-C-Al-Mn steel welds, Acta Mater. 50 (2002) 4763–4781. https://doi.org/10.1016/S1359-6454(02)00317-8.

[45] R. Trivedi, Interdendritic Spacing: Part Ii. a Comparison of Theory and Experiment., Metall. Trans. A, Phys. Metall. Mater. Sci. 15 A (1984) 977–982. https://doi.org/10.1007/bf02644689.

[46] W. Kurz, D.J. Fisher, Dendrite growth at the limit of stability: tip radius and spacing, Acta Metall. 29 (1981) 11–20. https://doi.org/10.1016/0001-6160(81)90082-1.

[47] R. Trivedi, P. Magnin, W. Kurz, Theory of eutectic growth under rapid solidification conditions, Acta Metall. 35 (1987) 971–980. https://doi.org/10.1016/0001-6160(87)90176-3.

[48] R. Trivedi, W. Kurz, Theory of Microstructural Development During Rapid Solidification., Acta Metall. 34 (1986) 260–267. https://doi.org/10.1007/978-94-009-4456-5_24.

[49] W. Kurz, R. Trivedi, Overview no. 87 solidification microstructures: recent developments a n d f u t u r e directions, Eng. Mater. Sci. Mater. 38 (1990) 1–17.

[50] J.A. Dantzig, M. Rappaz, Solidification, 2nd Editio, EPFL Press, 2016.

[51] K.D. Sisco, A. Plotkowski, Y. Yang, L. Allard, C. Fancher, C. Rawn, J.D. Poplawsky, R. Dehoff, S.S. Babu, Heterogeneous phase transformation pathways in additively manufactured Al-Ce-Mn alloys, J. Alloys Compd. 938 (2023) 168490. https://doi.org/10.1016/j.jallcom.2022.168490.

[52] R. Trivedi, W. Kurz, Dendritic Growth, Int. Mater. Rev. 39 (1994) 49–74.

[53] O. Grong, Metallurgical modelling of welding, 34 (1995) 289. https://doi.org/10.1016/1044-5803(95)80084-0.

[54] D. Rosenthal, Mathematical Theory of Heat Distribution During Welding and Cutting, Weld. J. 20 (1941) 220–234.

[55] A. Zhang, Y. Li, Thermal Conductivity of Aluminum Alloys—A Review, Materials (Basel). 16 (2023). https://doi.org/10.3390/ma16082972.

[56] S.L. Chen, S. Daniel, F. Zhang, Y.A. Chang, X.Y. Yan, F.Y. Xie, R. Schmid-Fetzer, W.A. Oates, The PANDAT software package and its applications, Calphad Comput. Coupling Phase Diagrams Thermochem. 26 (2002) 175–188. https://doi.org/10.1016/S0364-5916(02)00034-2.

[57] W. Cao, S.L. Chen, F. Zhang, K. Wu, Y. Yang, Y.A. Chang, R. Schmid-Fetzer, W.A. Oates, PANDAT software with PanEngine, PanOptimizer and PanPrecipitation for multi-component phase diagram calculation and materials property simulation, Calphad Comput. Coupling Phase Diagrams Thermochem. 33 (2009) 328–342. https://doi.org/10.1016/j.calphad.2008.08.004.

[58] EOS GmbH - Electro Optical Systems, EOS Aluminium AlSi10Mg, GPI Prototype Manuf. Serv. 49 (2014) 1–5. https://gpiprototype.com/pdf/EOS_Aluminium_AlSi10Mg_en.pdf.

[59] Y. Du, Y.A. Chang, B. Huang, W. Gong, Z. Jin, H. Xu, Z. Yuan, Y. Liu, Y. He, F.Y. Xie, Diffusion coefficients of some solutes in fcc and liquid Al: Critical evaluation and correlation, Mater. Sci. Eng. A. 363 (2003) 140–151. https://doi.org/10.1016/S0921-5093(03)00624-5.

[60] I. Rosenthal, R. Shneck, A. Stern, Heat treatment effect on the mechanical properties and fracture mechanism in AlSi10Mg fabricated by additive manufacturing selective laser melting process, Mater. Sci. Eng. A. 729 (2018) 310–322. https://doi.org/10.1016/j.msea.2018.05.074.

[61] T. Debroy, S.A. David, Physical processes in fusion welding, Rev. Mod. Phys. 67 (1995) 85–112. https://doi.org/10.1103/RevModPhys.67.85.

[62] M. Rappaz, S.A. David, J.M. Vitek, L.A. Boatner, Analysis of solidification microstructures in Fe-Ni-Cr single-crystal welds, Metall. Trans. A. 21 (1990) 1767–1782. https://doi.org/10.1007/BF02672593.

[63] F.G. Coury, E.L. Pires, W. Wolf, F.H. Paes de Almeida, A.L. Costa e Silva, W.J. Botta, C.S. Kiminami, M.J. Kaufman, Insight into the complex ternary phase behavior in Al-Mn-Ce alloys, J. Alloys Compd. 727 (2017) 460–468. https://doi.org/10.1016/j.jallcom.2017.08.136.

[64] K.D. Sisco, A. Plotkowski, Y. Yang, L. Allard, C. Fancher, C. Rawn, J.D. Poplawsky, R. Dehoff, S.S. Babu, Heterogeneous phase transformation pathways in additively manufactured Al-Ce-Mn alloys, J. Alloys Compd. 938 (2023) 168490. https://doi.org/10.1016/j.jallcom.2022.168490.

[65] D.J.S. Ferreira, B.N. Bezerra, M.N. Collyer, A. Garcia, I.L. Ferreira, The use of computational thermodynamics for the determination of surface tension and Gibbs–Thomson coefficient of multicomponent alloys, Contin. Mech. Thermodyn. 30 (2018) 1145–1154. https://doi.org/10.1007/s00161-018-0670-6.

[66] P.A.D. Jácome, D.J. Moutinho, L.G. Gomes, A. Garcia, The Application of Computational Thermodynamics for the Determination of Surface Tension and Gibbs-Thomson Coefficient of Aluminum Ternary Alloys, (2013) 871–876. https://doi.org/10.4028/www.scientific.net/MSF.730-732.871.

[67] P.M. Smith, M.J. Aziz, Solute trapping in aluminum alloys, Acta Metall. Mater. 42 (1994) 3515–3525. https://doi.org/10.1016/0956-7151(94)90483-9.

[68] M.J. Aziz, Model for solute redistribution during rapid solidification, J. Appl. Phys. 53 (1982) 1158–1168. https://doi.org/10.1063/1.329867.

[69] W.J. Boettinger, M.J. Aziz, Theory for the trapping of disorder and solute in intermetallic phases by rapid solidification, Acta Metall. 37 (1989) 3379–3391. https://doi.org/10.1016/0001-6160(89)90210-1.

[70] D.M. Herlach, Non-equilibrium solidification of undercooled metallic melts, Metals (Basel). 4 (2014) 196–234. https://doi.org/10.3390/met4020196.

[71] G.P. Ivantsov, The temperature field around a spherical, cylindrical, or pointed crystal growing in a cooling solution., Dokl. Akad. Nauk SSSR. 58 (1947).

[72] P. Mohammadpour, A. Plotkowski, A.B. Phillion, Revisiting Solidification Microstructure Selection Maps in the Frame of Additive Manufacturing, Addit. Manuf. 31 (2020) 100936. https://doi.org/10.1016/j.addma.2019.100936.

[73] H. Hartmann, P.K. Galenko, D. Holland–Moritz, M. Kolbe, D.M. Herlach, O. Shuleshova, Nonequilibrium solidification in undercooled Ti45Al55 melts, J. Appl. Phys. 103 (2008) 073509. https://doi.org/10.1063/1.2903920.

[74] M.F.A. J. C. Ion, K. E. Easterling, A Second Report on Diagrams of Microstructure and Hardness for heat-affected zones, Acta Met. 32 (1984) 1949–1962.